



Characterizing the Severe Turbulence Environments Associated With Commercial Aviation Accidents

Part II: Hydrostatic Mesobeta Scale Numerical Simulations of Supergradient Wind Flow and Streamwise Ageostrophic Frontogenesis

*Michael L. Kaplan, Allan W. Huffman, Kevin M. Lux, and Jeffrey D. Cetola
North Carolina State University, Raleigh, North Carolina*

*Joseph J. Charney
USDA/Forest Service, North Central Research Station, East Lansing, Michigan*

*Allen J. Riordan and Yuh-Lang Lin
North Carolina State University, Raleigh, North Carolina*

*Kenneth T. Waight III
MESO Inc., Raleigh, North Carolina*

The NASA STI Program Office . . . in Profile

Since its founding, NASA has been dedicated to the advancement of aeronautics and space science. The NASA Scientific and Technical Information (STI) Program Office plays a key part in helping NASA maintain this important role.

The NASA STI Program Office is operated by Langley Research Center, the lead center for NASA's scientific and technical information. The NASA STI Program Office provides access to the NASA STI Database, the largest collection of aeronautical and space science STI in the world. The Program Office is also NASA's institutional mechanism for disseminating the results of its research and development activities. These results are published by NASA in the NASA STI Report Series, which includes the following report types:

- **TECHNICAL PUBLICATION.** Reports of completed research or a major significant phase of research that present the results of NASA programs and include extensive data or theoretical analysis. Includes compilations of significant scientific and technical data and information deemed to be of continuing reference value. NASA counterpart of peer-reviewed formal professional papers, but having less stringent limitations on manuscript length and extent of graphic presentations.
- **TECHNICAL MEMORANDUM.** Scientific and technical findings that are preliminary or of specialized interest, e.g., quick release reports, working papers, and bibliographies that contain minimal annotation. Does not contain extensive analysis.
- **CONTRACTOR REPORT.** Scientific and technical findings by NASA-sponsored contractors and grantees.
- **CONFERENCE PUBLICATION.** Collected papers from scientific and technical conferences, symposia, seminars, or other meetings sponsored or co-sponsored by NASA.
- **SPECIAL PUBLICATION.** Scientific, technical, or historical information from NASA programs, projects, and missions, often concerned with subjects having substantial public interest.

TECHNICAL TRANSLATION. English-language translations of foreign scientific and technical material pertinent to NASA's mission.

Specialized services that complement the STI Program Office's diverse offerings include creating custom thesauri, building customized databases, organizing and publishing research results . . . even providing videos.

For more information about the NASA STI Program Office, see the following:

- Access the NASA STI Program Home Page at <http://www.sti.nasa.gov>
- Email your question via the Internet to help@sti.nasa.gov
- Fax your question to the NASA STI Help Desk at (301) 621-0134
- Telephone the NASA STI Help Desk at (301) 621-0390
- Write to:
NASA STI Help Desk
NASA Center for AeroSpace Information
7121 Standard Drive
Hanover, MD 21076-1320

NASA/CR-2003-212138



Characterizing the Severe Turbulence Environments Associated With Commercial Aviation Accidents

Part II: Hydrostatic Mesobeta Scale Numerical Simulations of Supergradient Wind Flow and Streamwise Ageostrophic Frontogenesis

*Michael L. Kaplan, Allan W. Huffman, Kevin M. Lux, and Jeffrey D. Cetola
North Carolina State University, Raleigh, North Carolina*

*Joseph J. Charney
USDA/Forest Service, North Central Research Station, East Lansing, Michigan*

*Allen J. Riordan and Yuh-Lang Lin
North Carolina State University, Raleigh, North Carolina*

*Kenneth T. Waight III
MESO Inc., Raleigh, North Carolina*

National Aeronautics and
Space Administration

Langley Research Center
Hampton, Virginia 23681-2199

Prepared for Langley Research Center
under Contract NAS1-99074

February 2003

Acknowledgments

This research has been funded under NASA Contract #NAS1-99074 and Subcontract #82U-7473-008 from the Research Triangle Institute. The authors wish to acknowledge the support of Dr. Fred H. Proctor, the NASA-Langley Technical Contract Monitor.

Available from:

NASA Center for AeroSpace Information (CASI)
7121 Standard Drive
Hanover, MD 21076-1320
(301) 621-0390

National Technical Information Service (NTIS)
5285 Port Royal Road
Springfield, VA 22161-2171
(703) 605-6000

Table of Contents

Abstract.....	1
1. Introduction.....	1
2. Model Simulation Experiments	3
2.1. Numerical Model.....	3
2.2. Severe Turbulence Case Studies.....	4
3. Converging Mesoalpha Scale Jet Stream Entrance Regions	4
4. Mesobeta Scale Centripetally Forced Ageostrophic Vertical Vorticity and Frontogenesis Between the Two Jet Streams	6
5. Summary and Discussion.....	9
6. References.....	10

List of Tables

Table 1. MASS Model (Version 5.13) Characteristics	12
Table 2. Data for the Four Hydrostatic Simulations.....	13
Table 3. Information About the Turbulence Encounter for Each of the Four Case Studies.....	13

List of Figures

Figure 1. NCEP Eta analysis observed total wind isotachs (dashed in ms^{-1}) and heights (solid in m) for the mandatory pressure level.....	14
Figure 2. NCEP height (light solid in m), ageostrophic wind vectors, and ageostrophic relative vorticity (negative dashed and positive dark solid in $\text{s}^{-1} \times 10^{-6}$)	17
Figure 3. NCEP height (light solid in m) and ageostrophic relative vorticity advection (negative dashed and positive dark solid in $\text{s}^{-2} \times 10^{-10}$).....	19
Figure 4. MASS 30-km simulated total wind isotachs (dashed in ms^{-1}), wind barbs (short barb = 5 ms^{-1} ; long barb = 10 ms^{-1} ; triangle = 50 ms^{-1}), and heights (solid in m).....	21
Figure 5. MASS 30-km simulated jet normal vertical cross sections of total wind isotachs (solid in ms^{-1}).....	23
Figure 6. MASS 30-km simulated jet normal vertical cross sections of potential temperature (solid in K) and isentropic potential vorticity (dashed in $\text{Kmb}^{-1}\text{s}^{-1} \times 10^{-6}$)	24
Figure 7. MASS 6-km simulated ageostrophic wind isotachs (solid in ms^{-1}) and vectors.....	25
Figure 8. MASS 6-km simulated vector resultant of the pressure gradient force and Coriolis force (thick) versus the total wind vectors (thin).....	26
Figure 9. MASS 6-km simulated Coriolis force vectors.....	27
Figure 10. MASS 6-km simulated cross-stream component and along-stream components of the pressure gradient force vectors.....	28
Figure 11. MASS 6-km simulated centrifugal force vectors	30
Figure 12. MASS 6-km simulated resultant of all four force vectors.....	31
Figure 13. MASS 6-km simulated v wind component divergence forcing function term in Miller's frontogenesis equation ($\text{km}^{-1}\text{s}^{-1} \times 10^{-8}$).....	32
Figure 14. MASS 6-km simulated total frontogenesis from Miller's (1957) equation ($\text{km}^{-1}\text{s}^{-1} \times 10^{-8}$).....	33
Figure 15. MASS 6-km simulated temperature (K).....	34
Figure 16. MASS 6-km simulated Montgomery stream function (light solid in m^2s^{-2}), ageostrophic wind vectors, and ageostrophic z-space relative vorticity ($\text{s}^{-1} \times 10^{-4}$).....	35
Figure 17. MASS 6-km simulated velocity divergence term in the ageostrophic z-space relative vorticity equation ($\text{s}^{-2} \times 10^{-9}$ in (a), $\text{s}^{-2} \times 10^{-7}$ in (b)) on an isentropic surface.....	36
Figure 18. MASS 6-km simulated Montgomery stream function (light solid in m^2s^{-2}) and the advection of ageostrophic z-space relative vorticity ($\text{s}^{-1} \times 10^{-8}$)	37

Abstract

Simulation experiments reveal key processes that organize a hydrostatic environment conducive to severe turbulence. The paradigm requires juxtaposition of the entrance region of a curved jet stream, which is highly subgeostrophic, with the entrance region of a straight jet stream, which is highly supergeostrophic. The wind and mass fields become misphased as the entrance regions converge resulting in the significant spatial variation of inertial forcing, centripetal forcing, and along- and cross-stream pressure gradient forcing over a mesobeta scale region. This results in frontogenesis and the along-stream divergence of cyclonic and convergence of cyclonic ageostrophic vertical vorticity. The centripetally forced mesoscale front becomes the locus of large gradients of ageostrophic vertical vorticity along an overturning isentrope. This region becomes favorable for streamwise vorticity gradient formation enhancing the environment for organization of horizontal vortex tubes in the presence of buoyant forcing.

1. Introduction

Turbulence has long represented one of the most demanding conceptual and forecasting challenges in meteorology. The fine spatial and temporal scale of turbulence and the coarse nature of atmospheric observations make even mapping the occurrence of turbulence, let alone forecasting it, extraordinarily difficult. Jet stream entrance regions have been known for many years to be preferred areas for turbulence (e.g., Reiter and Nania 1964; Mancuso and Endlich 1966; Roach 1970; Reed and Hardy 1972; Shapiro, 1976; Gidel and Shapiro 1979; Kennedy and Shapiro 1980; Uccellini et al. 1986; Keller 1990; Ellrod and Knapp 1992). In Kaplan et al. (2002) (Part I) this finding was reconfirmed in a 44 case study synoptic observational analysis of accident-producing turbulence case studies. However, the dynamical processes that make these jet entrance regions favored zones for severe turbulence are not well understood and, therefore, severe turbulence is not always accurately anticipated in advance as many well-organized jet entrance regions are largely devoid of even light turbulence whereas some produce extremely severe turbulence.

Previous studies (e.g., Uccellini et al. 1986; Keller 1990; Marroquin 1998) found that air parcels arriving from different regions in vertically sheared flows produce locally low Richardson

number or Richardson number tendency. Hence, they produce a region of significant turbulence probability in evolving frontal zones in confluent jet stream entrance regions. Low Richardson number and/or Richardson number tendency indicated that the greatest shear and buoyancy potential for turbulence kinetic energy generation existed in the frontal zones accompanying jet entrance regions. However, forecasting indices, which typically rely solely on these Richardson number-based fields, are rarely employed operationally. These indices alone are not always successful at discriminating between turbulent and nonturbulent regimes because of the very fine scale structure of the frontal zones that organize the turbulent event, i.e., the organizing circulation is so fine that only the environment that produces it can be sensed or simulated. Rarely can turbulence be accurately forecasted operationally without the inclusion of kinematic forcing, e.g., the velocity deformation, potential vorticity, and/or velocity divergence (Ellrod and Knapp 1992; Sharman et al. 2000). As an example, a useful index employed by the National Weather Service is the Ellrod and Knapp index, which is simply the product of the deformation and the vertical wind shear. The Intergrated Turbulence Forecasting Algorithm (ITFA) index, operationally employed at the National Center for Atmospheric Research, is a synthesis of many fields that are explicit functions of both Richardson number and

flow kinematics. Hence, given that both unique kinematic as well as vertical wind shear and buoyancy forcing are diagnosed in regions of turbulence, there can be a great deal of uncertainty concerning what processes accompanying jet entrance regions consistently organize the environment that creates turbulence of greater than moderate intensity. Adding to the theoretical complexity, Knox (1997) noted how inertial instability and geostrophic adjustment are likely maximized in many case studies where clear air turbulence may occur. Since inertial instability can be directly related to low potential vorticity and low Richardson number, which are typical of anticyclonically shearing jet streams embedded within strong frontal systems, it represents yet another possible mechanism of turbulence development related to jet entrance regions, fronts, low Richardson number, deformation, and vorticity (Stone 1966). Thus, buoyancy-based forcing, shear-based forcing, kinematics-based forcing, and complex combinations thereof can be related to characterizing the environment that organizes turbulence but may or may not be a discriminating condition for the development of severe accident-producing turbulence. This issue of unambiguously discriminating when and where an environment will organize fine scale severe turbulence represents an unsolved problem in applied meteorology.

Recently, Andreassen et al. (1998) presented idealized numerical simulation results and Clark et al. (2000) presented real data numerical simulation-derived as well as observationally derived evidence of vortex tubes in the vicinity of severe turbulence. Both groups hypothesize the possible mutual interaction of vortex tubes at the mesoscale and microscale as key mechanisms in the organization of severe clear air and terrain-induced turbulence. Regions of strong vertical vorticity at the mesoscale often produce microscale maxima of horizontal vorticity due to flow blocking and/or channeling near terrain or due to local solenoidal forcing. Both sets of simulations unambiguously indicate that a scale contraction process can focus significant rotation (vortex tubes) into a highly specific region, which could, in theory, produce a flow obstacle causing

extreme turbulence in the path of an aircraft. This is most likely to occur if one observes a very intense vertical transport of rotation in the form of vortices. However, it has never been unambiguously and conclusively proven that vortices cause the type of turbulence that results in aviation accidents, though a case was made for such by Parks et al. (1994). Nevertheless, Clark et al. (2000) provided unambiguous evidence that observed turbulence and vortex tube generation was collocated for a case of mountain turbulence.

There are two fundamental questions to be asked. Are clear air and convective turbulence, which often occur displaced from mountains, the result of intense vortex tube formation? How do they evolve within favored regions accompanying jet stream entrance areas where strong three-dimensional wind shears, low buoyancy, and large values of potential vorticity exist, but where no fixed blocking mechanism is in place? Clearly, there is a need for a coherently crafted multiscale theory or paradigm based on several real-data observational analyses and multiscale numerical simulations. This could offer improved understanding of how preferred zones for severe turbulence are organized in both convection and clear air. If such a paradigm were developed, the result would be the formulation of an algorithm employed in turbulence forecasting that represents a potential improvement to the state-of-the-science. It is the goal of this report, Part II, to build on the findings presented in Part I by synthesizing such a coherent original paradigm at the hydrostatic subsynoptic scales of motion whose end product is to improve the accuracy with which accident-producing turbulence is predicted in both convection and clear air. The organization of streamwise gradients of ageostrophic relative vorticity in the preturbulent environment is key to this paradigm. In subsequent reports, i.e., Parts III and IV, we will, first, demonstrate the theory supporting a nonhydrostatic sequence of processes that organizes an environment favorable for horizontal vortex tube formation from streamwise gradients of hydrostatic ageostrophic relative vorticity. Second, we will endeavor to demonstrate the real-time operational application of an index, which is based on this theory, for a wide variety of

moderate-severe mountain, clear air, and, primarily, convective turbulence case studies.

In this paper we will utilize mesoalpha and mesobeta scale hydrostatic numerical simulations of recurring multiscale dynamical processes that result in accident-producing turbulence. The focus will be on turbulence in proximity to deep moist convection; however, a clear air turbulence case study is also examined in an effort to show how the hydrostatic precursor environment for both severe clear air turbulence (CAT) and convectively induced turbulence (CIT) are quite similar. That is not to say that we are claiming to develop a paradigm that includes a scale contraction process achieving the turbulent “event.” Our goal is to develop a paradigm that synthesizes a recurring sequence of processes from the subsynoptic to mesobeta scales of atmospheric motion. This paradigm will define the roles of frontogenesis, vorticity tendencies, and more importantly ageostrophic motions in focusing a streamwise relative vorticity gradient maximum accompanying an ageostrophically forced front in the location of an observed severe turbulence event. We seek to understand the larger scale organizing environment for severe turbulence. The seminal flow regime that is key to the aforementioned paradigm is associated with supergradient wind flow. By supergradient wind flow we mean flow that significantly exceeds gradient wind balance due to the large magnitude of the centrifugal force. Supergradient wind flow facilitates a rapid increase in mesoscale frontogenetical forcing in a rotational environment prior to the development of nonhydrostatic convective forcing. By frontogenetical forcing we mean nonlinear processes that increase the magnitude of a streamwise mesoscale front. Supergradient and unbalanced supergradient wind flows are very effective at increasing streamwise wind perturbations as the ageostrophic confluence accompanying said flows is often frontogenetical, thus producing along-stream temperature (density) gradients in proximity to along-stream mass (pressure) perturbations. From an isentropic perspective this represents the convergence of streamwise ageostrophic relative vorticity on a sloping isentropic surface in a buoyant environment. Such a circulation estab-

lishes an environment that is favorable for the forcing of x-space and y-space vorticity through streamwise gradients of the u, v, and w wind components, i.e., ageostrophic flow conducive to microscale vortex tube formation.

In section 2 we briefly describe the four case studies to be simulated that are representative of aircraft accident-producing clear air and convective turbulence analogous to those analyzed in Part I. We also describe the numerical model and simulation experiments employed to understand the key sequence of ageostrophic circulations, which we describe subsequently. Section 3 focuses on the mesoalpha scale (≈ 500 km) structure of the intersecting confluent jet stream entrance regions, which organize the key hydrostatic severe turbulence-forcing processes in section 4. It is the highly ageostrophic state created by these juxtaposed jet entrance region circulations that organize the potential for supergradient wind flow that leads to mesobeta scale ageostrophically forced frontogenesis accompanying streamwise ageostrophic relative vorticity. In section 4 we describe stage 1 of the overall paradigm, wherein mesobeta scale (≈ 100 km) ageostrophic forcing organizes frontogenesis. This involves the development of supergradient wind flow within two laterally and vertically juxtaposed jet entrance region circulations. In section 5 we summarize the new hydrostatic component of the severe turbulence-producing paradigm.

2. Model Simulation Experiments

2.1. Numerical Model

The numerical model to be employed in the hydrostatic real data simulation experiments is the Mesoscale Atmospheric Simulation System (MASS) (Kaplan et al. 2000). Table 1 describes the characteristics of the hydrostatic version 5.13. The hydrostatic simulations, to be described in subsequent sections, are the 30-km (coarse) and 6-km (fine) mesh simulations. Initial and time dependent lateral boundary conditions are derived from the National Weather Service (NWS) Eta analyses for the coarse mesh simulation. All consecutive finer scale simulations, which are nested,

derive their initial and time dependent lateral boundary conditions from the next coarser mesh simulation. Climatological soil moisture, climatological sea surface temperatures, and an average of both silhouette and envelope terrain are utilized in all four simulated case studies. Representative matrix sizes employed, initialization times, and other key details are defined in table 2.

2.2. Severe Turbulence Case Studies

Two of these four real data case studies represent accident-producing and severe turbulence events as described in the archives of the National Transportation Safety Board (NTSB) analogous to those described in Part I. Table 3 defines the details of the turbulence encounter times and locations and figure 1(e) graphically depicts their locations. One of the four case studies unambiguously occurs in clear air about 50 km southwest of Cape Girardeau, Missouri (CGI) at 1453 UTC 28 January 1997 at nearly 7000 m elevation. This represents one of the two accident case studies. The other three case studies all are in proximity to moist convection. Two of these involve deep moist convection, the first of which occurred about 60 km southwest of Cross City, Florida (CTY) at 0045 UTC 2 October 1997 at around 10000 m, which is the second accident case study. The other deep convection case is NASA-Langley Flight Experiment 191 about 90 km southwest of Valdosta, Georgia (VAD) at 1844 UTC 14 December 2000 at around 10000 m. The fourth case study represents an FAA Flight Operations Quality Assurance (FOQA) case study wherein equipment recording severe turbulence was on board a commercial aircraft. This is the only low-level turbulence case study, occurring at around 2400 m at 1931 UTC 13 January 2000 nearly 50 km southeast of Wilmington, Delaware (ILG) in proximity to relatively shallow convection.

All case studies contain the same general synoptic structure representative of most of the 44 case studies whose evaluation was presented in Part I, namely, a jet entrance region location, upstream curvature accompanying streamwise gradients of ageostrophic relative vorticity,

nearby convection (except in the clear air case study), upward synoptic scale vertical motion, low absolute vorticity, horizontal cold air advection, and synoptic scale leftward-directed ageostrophic flow. The VAD and ILG case studies likely could have been accident-producing events as defined in Part I where there were no special circumstances involved in the observation of severe turbulence, which did occur. CGI differs from the other three case studies in that there was no moist convection near the event. These four case studies were not included in the 44 case study sample described in Part I. They were selected for the comprehensive modeling studies, described in this paper and in Part III, because of the detailed flight data recorder information that NASA was able to access for these case studies from either the NTSB or actual experimental research flights. Almost all of the 44 case studies described in Part I did not have any accessible high quality flight data recorder information. Hence, the validation of the modeling of these four case studies from subsequent large eddy simulation (LES) studies is facilitated by microscale observations of the dynamics preceding the turbulent event as diagnosed from the flight data recorder information.

3. Converging Mesoalpha Scale Jet Stream Entrance Regions

Figures 1 through 3 depict the observed synoptic National Centers for Environmental Prediction (NCEP) Eta analysis fields valid at the rawinsonde time immediately preceding the severe turbulence event with the exception of the ILG case study where the data follow the event. The times of the observational analyses are the closest possible to the times of the accidents. Figure 4 depicts important 30-km simulated dynamical fields accompanying the jet streams for all four case studies while figures 5 and 6 focus on the two case studies with the strongest jet streams. These figures of simulated data include the horizontal cross sections of winds and heights near the elevation of severe turbulence (fig. 4) as well as perpendicular vertical cross sections of winds (fig. 5) and isentropic potential vorticity (IPV) (fig. 6). The times of each simulated cross section

are about one to two hours prior to the observed severe turbulence event. These case studies vary substantially in the intensity of the mesoalpha scale jet streams near the accident locations, with the CGI case study intensity being the strongest; but there are many common signals among the jet streams. First, they represent locations of three-dimensional transition between two jet stream entrance regions and their supporting baroclinic zones. The northern stream is curved, weaker, and lower in elevation whereas the southern stream is straighter, stronger, and higher in elevation (note figs. 1 and 4). Second, these jet stream entrance regions indicate highly confluent ageostrophic flow with leftward-directed ageostrophy in the southern jet stream and rightward-directed ageostrophy in the northern jet stream, as can be seen in the ageostrophic vectors depicted in figure 2 and inferred from the wind and height data depicted in figure 4. Third, the vertical structure depicted in figure 5 indicates a wind maximum above and just upstream from the level of the accident with a region of stronger winds extending downward through the level of the accident; this indicates the proximity of the deep jet streams that phase above the same location in the vertical. Fourth, the IPV maximum in figure 6, which is in proximity to the accident location in both space and time, slopes downward as a separate weaker maximum and is detached from a more classic stratospheric IPV maximum accompanying a tropopause fold. The IPV maximum near the level of the severe turbulence event is located within the transition zone between the jet stream entrance regions. The shallower location and separate structure of these IPV maxima, which are located near the accident, suggest a separate highly ageostrophic organizational process for the lower level and much smaller IPV maximum as these features are not directly accompanying the deeper stronger quasi-geostrophic tropopause folding event accompanying the injection of large-IPV stratospheric air. This indicates the possibility that a separate downstream and lower level frontogenetical circulation is being established that is detached from the quasi-geostrophic front supporting the tropopause fold. Additionally, the ageostrophic circulation vectors (inferred from fig. 2) indicate highly different circulations

in the two jet stream entrance regions wherein a more dominant thermally indirect circulation exists poleward of a more dominant thermally direct circulation.

The most significant signals of the intersecting entrance regions and secondary IPV maxima are evident in the CGI and ILG case studies. Note, in particular, in these two case studies how the ageostrophic confluence is established between Illinois and Arkansas and Pennsylvania and Virginia, for CGI and ILG, respectively. The secondary IPV maxima align rather closely with the accident location between these ageostrophic confluent regions. Furthermore, the ageostrophic vectors are separated by a region of highly curved flow in all four case studies but most notably in the CGI and ILG case studies. Finally, and most dramatically, figures 2 and 3 indicate the dominance of streamwise gradients of ageostrophic relative vorticity and ageostrophic relative vorticity advection in all four case studies. The streamwise adjustments typically exceed the cross-stream adjustments in magnitude near the accident location. Additionally, a close look at the CGI and ILG case studies (the strongest case studies) indicates a signal of an observed ageostrophic cyclonic circulation in the vectors depicted in figure 2. This circulation is centered roughly on Missouri for CGI in figure 2(a) and just offshore from the Middle Atlantic coast southeast of ILG in figure 2(b). This represents the juxtapositioning of a southern stream and its ageostrophic circulation and a northern stream and its ageostrophic circulation within an environment dominated by curved cyclonic ageostrophic flow.

Juxtapositioning these two very different ageostrophic circulations is effective at forcing a region of ageostrophic confluence in proximity to the cold air that is typically located within the poleward jet stream entrance region. Hence, it establishes a favorable environment for ageostrophically forced frontogenesis and fine-scale streamwise temperature and density gradients. These observed and simulated structures are consistent in a synoptic sense with the confluence of two jet entrance regions occurring ahead of a

region of curved flow. Synoptic analyses of IPV and ageostrophic circulation vectors (not shown) can not match the necessary detail that is required to define these features inherent in the 30-km simulations, thus indicating how subsynoptic and ageostrophic these features are.

4. Mesobeta Scale Centripetally Forced Ageostrophic Vertical Vorticity and Frontogenesis Between the Two Jet Streams

All of the analyses discussed in this section are performed employing the fields simulated with the 6-km hydrostatic version of the numerical model. Figure 7 depicts the simulated ageostrophy in the two strongest case studies on the pressure surface that is nearly coincident with the level of the accident. This ageostrophy is located in the curved flow where the trough and the southern jet entrance region are juxtaposed. In all four case studies the simulated ageostrophic wind vectors have a similar pattern, albeit a large variation of magnitude, from one case study to the other. This pattern of ageostrophic flow is somewhat like a positively tilted cyclonic circulation roughly centered on the accident location. To the north and west of the accident location the ageostrophic wind vectors are directed upstream of the large scale wind flow and to the south and east of the accident location they are directed downstream of the large scale wind flow. This is analogous to a positively tilted highly confluent cyclonic circulation with a bias towards leftward-directed cross-stream ageostrophic flow. Not all of the vectors conform strictly to this state of ageostrophy, as the shorter the radius of curvature and the stronger the momentum in the merging jet streams the more the vectors are likely to split the flow into upstream and downstream ageostrophic wind components; note the CGI and ILG case studies. This simulated pattern, depicted in figure 7, can be roughly compared to the observed ageostrophic vectors depicted in figures 2(a) and 2(b) wherein the cyclonic ageostrophic circulation with upstream-directed flow to the northwest and downstream-directed flow to the southeast is evident surrounding Missouri in figure 2(a) and just

offshore southeast of the DelMarVa Peninsula in figure 2(b). In the CTY and VAD case studies (not shown) the wind vectors are not sufficiently ageostrophic to unambiguously split the flow and produce the cyclonic circulation as in the CGI and ILG case studies, although a weak signal of the split flow does exist. The fact that any vectors conform to this state of imbalance is an indication of just how misphased the pressure gradient and Coriolis forces are as they fail to directly balance one another by large magnitudes. This lack of direct balancing can be better visualized in figure 8 by comparing the vector resultant of the ageostrophic flow not including the centrifugal force, i.e., the acceleration vector for straight flow (combined pressure gradient and Coriolis force) with the total wind vectors. This pattern represents subgeostrophic flow on the upstream (generally north and west) side of the accident and supergeostrophic flow on the downstream (generally south and east) side of the accident. The cyclonic rotation of the combined pressure gradient force and Coriolis force vectors relative to the trough structure in the total wind velocity vector can be seen in figure 8. This pattern is in place prior to any forcing from moist or dry convection. This type of misphasing between the pressure gradient force and Coriolis force favors a flow in which there is a net acceleration directed downstream and to the right of the split in the wind flow well ahead of the trough, and a net acceleration directed upstream and to the left of the split in the wind flow within the trough. This split in the ageostrophic flow produces ageostrophic vectors directed in large part along the stream but in opposite directions. When curvature of the wind flow is added to the imbalance of forces, the centrifugal force is very effective at enhancing the net accelerations primarily directed downstream but with the maximum shifted upstream from the Coriolis force. As a matter of fact, the most highly curved flow is situated between the upstream-directed maxima in the pressure gradient force and downstream-directed maxima in the Coriolis force, thus dominating the transition between the two forces.

To diagnose the specific cause of this pattern of extreme ageostrophy, resulting in large part

from the flow curvature, we calculate the Eulerian imbalance of forces for inviscid flow at staggered grid points on the same pressure surfaces as the previous ageostrophic wind vectors for the CGI and ILG case studies (focusing on the case studies with the strongest signals). This accelerative signal in the imbalance of forces is strongest in CGI and ILG but also apparent to a lesser extent in the deeper stronger convective events, i.e., CTY and VAD (not shown). These imbalance-of-forces fields for the CGI and ILG case studies are depicted in figures 9 through 12. The purpose of this calculation is to determine the dominant instantaneous forcing at each grid point surrounding the accident location. All calculations of the centrifugal force are based on the curvature of a parcel trajectory as defined in Dutton (1976). These figures indicate that the upstream subgeostrophy is the result of the strong upstream-directed normal and tangential components of the pressure gradient force accompanying the northern curved and highly confluent jet stream entrance region (fig. 10). The trough structure and its positively tilted and highly confluent height gradient forces the pressure gradient force vector, the resultant of cross-stream and along-stream components, to be directed to the north-northwest to west-northwest. This orientation is consistent with a strong (as in subgeostrophic flow) streamwise component of the pressure gradient force accompanying the curved height field. The downstream-directed supergeostrophic flow is coincident with the Coriolis force maxima accompanying the southern straight jet stream entrance region where inertia is very strong (fig. 9). These two force maxima are spatially separated rather than balancing one another, reflecting the proximity of a curved height field and straight jet stream flow. The region between the two aforementioned force maxima is generally a maximum of the centrifugal force and substantial centrifugal force variation (fig.11) as the radius of curvature is small and varying and the magnitude of the velocity is large. The resultant of all three forces depicted in figure 12 is analogous to the pattern of ageostrophy depicted in figure 7, i.e., an acceleration vector that includes curvature. Most important is the fact that the maxima of the along-stream pressure gradient force, cross-stream

pressure gradient force, Coriolis force, and centrifugal force are all misphased, which facilitates the local variation of ageostrophy and the local dominance of centripetal flow between the large leftward and upstream-directed maxima of the pressure gradient force and large rightward and downstream-directed maxima of the Coriolis force. For example, note how the centrifugal force vector in figure 11 is longer than the combined pressure gradient force terms and Coriolis vector resultant in figure 8 over the region between southern Missouri and western Kentucky for the CGI case study and over the region between northeastern Maryland, northern Delaware, and southwestern New Jersey for the ILG case study. The dominance of centripetal forcing is not as obvious in the CTY and VAD case studies, however, the pattern is similar (not shown).

The dominance of centripetal flow between the maxima of the other forces produces a narrow region where the flow may be termed supergradient (note figs. 10 and 11). Supergradient flow represents flow exceeding gradient wind balance due to the large centripetal forcing, or flow having a small radius of curvature with large wind values. This supergradient flow is a result of the misphasing among all three terms established by the juxtaposition of these unique jet stream entrance region configurations and covers a mesobeta scale region. The centrifugal force dominates any balance among the three forces during inviscid flow allowing variation in curvature effects to control the forcing over a very limited region during a short time period. The local supergradient flow maximum is very close to the turbulence accident location in all four case studies. The result is that the total wind vertical vorticity gradient in this highly ageostrophic state is not collocated with the geostrophic wind vertical vorticity gradient, thus initiating the process of streamwise gradients of ageostrophic vertical vorticity. Centripetal forcing produces the streamwise shears that organize an ageostrophic vertical vorticity maximum.

Mesobeta scale spatial variations in the aforementioned centripetal forcing result in narrow zones of enhanced velocity convergence and

divergence as the ageostrophic vertical vorticity gradients sharpen over time. As such, one would expect that this pattern of ageostrophy, in proximity to the jet stream entrance region thermal variation, would represent a favored region for mesoscale rotational/ageostrophically forced frontogenesis because thermal gradients and velocity convergence due to ageostrophic flow are large and coexist here. The aforementioned juxtaposition of ageostrophic confluent flow and thermal variation that is required to produce frontogenesis by the key forcing functions in Miller's (1948) equation can be inferred from equation (1):

$$F = -\frac{1}{|\nabla\theta|} \left[\frac{\partial\theta}{\partial x} \left(\frac{\partial u}{\partial x} \frac{\partial\theta}{\partial x} + \frac{\partial u}{\partial y} \frac{\partial\theta}{\partial y} \right) + \frac{\partial\theta}{\partial y} \left(\frac{\partial v}{\partial x} \frac{\partial\theta}{\partial x} + \frac{\partial v}{\partial y} \frac{\partial\theta}{\partial y} \right) + \frac{\partial\theta}{\partial p} \left(\frac{\partial\omega}{\partial x} \frac{\partial\theta}{\partial x} + \frac{\partial\omega}{\partial y} \frac{\partial\theta}{\partial y} \right) \right] \quad (1)$$

As the ageostrophy increases along the curved flow stream, note the dominance of the convergence term in equation (1) that primarily accompanies the streamwise variation of the predominantly ageostrophic v wind component, depicted in figure 13, within this region of strong centripetal forcing variation. This dominant ageostrophic contribution is coincident with the short scale length of the variation in centripetal forcing. This large streamwise variation of the ageostrophic wind is nearly coincident with the total frontogenesis in figure 14, which, in turn, passes very close to if not over the accident location in all four case studies. It is this particular forcing function phasing with the larger scale entrance region variation in the predominantly streamwise temperature pattern in figure 15 that dominates frontogenesis. In this region, the x -space variation of the v ageostrophic wind velocity component consistent with the shearing deformation terms (not shown in fig. 15), is much weaker in magnitude than the x -space variation of the u ageostrophic wind velocity component and the y -space variation of the v ageostrophic wind velocity component, i.e., the stretching deformation terms and their correlation with the NNW-SSE jet entrance region's temperature gradient (note figs. 13 and 15). Con-

fluence of the ageostrophic v wind component in the along-stream plane is coincident with the streamwise (WNW-ESE) component of the temperature variation, thus producing the dominant mesoscale frontogenetical forcing mechanism of the two deformation terms in Miller's equation. The role of stretching deformation highlights the importance of the confluent cold trough as well as the large streamwise momentum variation typical of supergradient wind flow. The location of the confluent ageostrophically forced front is coincident with the transition from upstream-directed subgeostrophy and downstream-directed supergeostrophy, or very close to the significant local variation of centripetal forcing between the regions of subgeostrophy and supergeostrophy, i.e., the region of supergradient wind flow. Hence, the frontogenesis is strongly controlled by the streamwise mesoscale variation of the curvature accompanying the ageostrophic wind and is roughly coincident with the accident location. This ageostrophic confluence results from the lateral variation of centripetal accelerative flow, which is allowed to occur in a largely unperturbed manner by the separated maxima of the pressure gradient force (directed upstream) and Coriolis force (directed downstream) in this uniquely determined confluence zone of two jet stream entrance regions. Centripetal forcing establishes the region of meridional confluence as the pressure gradient and Coriolis forces are directed at substantial angles to the centrifugal force by the confluence of two different jet stream entrance regions, i.e., one stream supplying curvature and cold air and a second stream supplying zonal momentum. The streamwise variation of the gradient of the ageostrophic vertical vorticity is coincident with the ageostrophic stretching deformation maxima. Hence, mesoscale frontogenesis in the curved flow acts to sharpen the angle between the streamwise ageostrophic vertical vorticity gradient and Montgomery stream function gradient as the slope of the isentropic surface, which accompanies mesoscale frontogenesis, steepens. Frontogenesis and steepening isentropes become collocated with the streamwise ageostrophic vorticity gradient.

The narrow (≈ 50 to 100 km) streamwise ageostrophically forced front is therefore a region

of intensifying ageostrophic vertical vorticity gradients on sloping isentropic surfaces. Figure 16 depicts the ageostrophic vertical relative vorticity on the key isentropic surface passing through the location of observed turbulence in the CGI and ILG case studies. Evident is the focusing of an ageostrophic vertical vorticity gradient maximum near the turbulence location consistent with the narrow maximum of frontogenesis. This maximum in the gradient of ageostrophic vertical vorticity is also coincident with the maximum in ageostrophic deformation. This ageostrophic vorticity maximum is largely the result of the substantial velocity convergence in the centripetally forced streamwise confluence zone between the maxima of the pressure gradient and Coriolis forces. The variation in centripetal forcing, its subsequent velocity convergence, and ageostrophic vertical vorticity are all phasing to produce a mesobeta scale region of rapid transition of density accompanying the newly formed front (note figs. 14 and 15). As can be seen in figures 16 and 18, the location of the maxima of increasing ageostrophic vertical vorticity in time is close to the convergence and stretching term maxima in the vertical vorticity equation calculated with the ageostrophic component of the wind in figure 17. As such the vertical vorticity of the total wind and the vertical vorticity of the geostrophic wind can become separated with cyclonic ageostrophic vorticity shifted downstream relative to cyclonic geostrophic vorticity. This produces a separate region of streamwise vertical vorticity gradient formation ahead of the larger scale trough within the newly formed front's sloping isentropes where increased buoyancy is being organized as well. Consistent with this are the maxima in variation of the advection of ageostrophic relative vorticity over southeastern Missouri and southwestern New Jersey for the CGI and ILG case studies, respectively depicted in figure 18. These are regions becoming dominated by a flow favoring streamwise ageostrophic vorticity advection. As such, the environment is becoming more conducive to horizontal vortex tube formation if a local source of buoyancy can tilt and converge said vertical vorticity into horizontal vorticity.

5. Summary and Discussion

The processes that separate the total wind vertical vorticity and geostrophic wind vertical vorticity maxima and create the intense streamwise front and accompanying ageostrophic vorticity gradients depicted in figures 15 and 16 have their roots in the mesoalpha jet stream structures. The juxtaposition of highly curved flow, cold advection, and strong inertial forcing set up an imbalance of forces that is highly ageostrophic. The signal of this ageostrophy is the fine scale confluence, which contracts the scale of the centripetally forced front and its attendant streamwise vertical vorticity maxima. This sequence of events is essentially about separating the geostrophic vertical vorticity from the total wind vertical vorticity, creating the ageostrophic vertical vorticity on a sloping isentropic surface, i.e., the newly formed ageostrophically forced front and streamwise vorticity maxima. As such, the cross product formed by the gradients of the total wind vertical vorticity and the pressure gradient force should be large, indicating just how the ageostrophic front focuses this separation (note equation (2)). The pressure gradient force is oriented progressively more orthogonal to the gradients of ageostrophic vertical vorticity:

$$\text{NCSU} = \nabla \zeta_{\theta} \times \nabla M_{\theta} \quad (2)$$

This separation of the horizontal pressure gradient force from the total wind vertical vorticity can be a multiscale indicator of the evolving ageostrophic frontogenesis and the convergence of vertical vorticity on folding isentropic surfaces. Hence, this separation is conceivably a useful forecasting tool for the prediction of regions of severe turbulence potential. In its most basic representation, the separation is the location of most rapidly increasing streamwise vorticity gradient in a progressively more buoyant environment accompanying the overturning isentropes. The increase of streamwise vertical vorticity will be where the total frontogenesis and ageostrophic vorticity are becoming collocated, as can be

inferred from figures 13 through 18. The stream-wise density gradient accompanying the newly formed front and ageostrophic vorticity maximum are becoming orthogonal to the streamwise pressure gradient force ahead of the trough in the mass field.

The hydrostatic mesoscale sequence of events hypothesized to maximize the potential for both clear air and convective turbulence follows:

- (1) Two jet stream entrance regions become juxtaposed resulting in proximity between curved flow in a baroclinic zone and stronger straight advective flow, which vary substantially in magnitude in the vertical.
- (2) The misphasing of the along-stream and cross-stream maxima in the pressure gradient force, the centrifugal force, and the Coriolis force at the interface of the two jet stream entrance regions produces a local region of highly confluent ageostrophic curved flow that may be supergradient.
- (3) The confluence resulting from the variation of the streamwise wind component in this highly ageostrophic “stretched” state produces a mesobeta scale frontal zone and maximum in ageostrophic vertical vorticity.
- (4) The increasingly streamwise-oriented front becomes the locus of three-dimensional wind gradients, which are available for tilting, and vertical convergence into horizontally intensifying vortex tubes if significant buoyant lifting occurs.

This hydrostatic sequence of events results in the focusing of maxima of kinematic forcing, frontogenesis, and minima in Richardson number in the same place and the same time as the isentropic surface folds in proximity to strong two-dimensional rotation about the vertical axis. From a physical perspective, this process represents the isentropic surfaces folding over in proximity to strong gradients of ageostrophic vertical vorticity.

Presumably, the turbulent event accompanies the breakdown of the flow established by this complex sequence of dynamical processes and the resulting sequence of nonhydrostatic adjustments that focuses vorticity (vortex tubes) in both of the remaining horizontal (x- and y-space) planes of motion. A potentially useful turbulence forecasting index that reflects these dynamics is developed and is based on the misphasing of the geostrophic and total wind vertical vorticity gradients on an isentropic surface. Here the pressure gradient force is orthogonal to the gradient of vertical vorticity, thus collapsing the scale of the front and streamwise vorticity gradients. The downscale growth of ageostrophy and frontogenesis is nothing more than the increasing orthogonality between the streamwise pressure gradient force and gradient of total wind vertical vorticity.

In a subsequent report, i.e., Part III, the second and third stages of the paradigm are described using both nested-grid real data nonhydrostatic simulations and idealized nonhydrostatic simulations of intense convectively forced three-dimensional circulations. The scale contraction of the turbulence index from its hydrostatic maxima to finer scale nonhydrostatic maxima will be described in depth in Part III wherein buoyancy can lead to a set of adjustments that tilt and converge the newly formed streamwise vertical vorticity gradients at the hydrostatic scale of motion into horizontal vortex tubes at the nonhydrostatic scale of motion.

6. References

- Andreassen, O.; Hvidsen, P. O.; Fritts, D. C.; and Arendt, S. 1998: Vorticity Dynamics in a Breaking Internal Gravity Wave. Part I: Initial Instability Evolution. *J. Fluid. Mech.*, **367**, 27–46.
- Clark, T. L.; Hall, W. D.; Kerr, R. M.; Middleton, D.; Radke, L.; Martin, Ralph F.; Nieman, P. J.; and Levinson, D. 2000: Origins of Aircraft-Damaging Clear Air Turbulence During the 9 December 1992 Colorado Downslope Windstorm: Numerical Simulations and Comparison to Observations. *J. Atmos. Sci.*, **57**, 1105–1131.

- Dutton, J. A. 1976: Aperiodic Trajectories and Stationary Points in a Three-Component Spectral Model of Atmospheric Flow. *J. Atmos. Sci.*, **33**, August, 1499–1504.
- Ellrod, G. P.; and Knapp, D. I. 1992: An Objective Clear-Air Turbulence Forecasting Technique: Verification and Operational Use. *Wea. Forecasting*, **7**, 150–165.
- Endlich, R. M. 1964: The Mesoscale Structure of Some Regions of Clear-Air Turbulence. *J. Appl. Meteor.*, **3**, 261–276.
- Gidel, L. T.; and Shapiro, M. A. 1979: The Role of Clear Air Turbulence in the Production of Potential Vorticity in the Upper Tropospheric Jet Stream-Frontal Systems. *J. Atmos. Sci.*, **36**, 2125–2138.
- Kaplan, M. L.; Lin, Y.-L.; Charney, J. J.; Pfeiffer, K. D.; Ensley, D. B.; DeCroix, D. S.; and Weglarz, R. P. 2000: A Terminal Area PBL Prediction System at Dallas-Fort Worth and Its Application in Simulating Diurnal PBL Jets. *Bull. Amer. Meteor. Soc.*, **81**, 2179–2204.
- Kaplan, M. L.; Huffman, A. W.; Lux, K. M.; Charney, J. J.; Riordan, A. J.; and Lin, Y.-L. 2002: Characterizing the Environment Organizing Severe Accident-Producing Turbulence. Part I: 44 Case Study Synoptic Observational Analyses. NASA CR 211918.
- Keller, J. L. 1990: Clear-Air Turbulence as a Response to Meso- and Synoptic-Scale Dynamical Processes. *Mon. Wea. Rev.*, **118**, 2228–2242.
- Kennedy, P. J.; and Shapiro, M. A. 1980: Further Encounters With Clear Air Turbulence in Research Aircraft. *J. Atmos. Sci.*, **37**, 986–993.
- Knox, J. A. 1997: Possible Mechanisms of Clear-Air Turbulence in Strongly Anticyclonic Flows. *Mon. Wea. Rev.*, **125**, 1251–1259.
- Mancuso, R. L.; and Endlich, R. M. 1966: Clear-Air Turbulence Frequency as a Function of Wind Shear and Deformation. *Mon. Wea. Rev.*, **94**, 581–585.
- Marroquin, A. 1998: An Advanced Algorithm To Diagnose Atmospheric Turbulence Using Numerical Model Output. Preprints, *16th AMS Conference on Weather Analysis and Forecasting*, 11–16 January, 79–81.
- Miller, J. E. 1948: On the Concept of Frontogenesis. *J. Meteor.*, **5**, 169–171.
- Parks, E. K.; Wingrove, R. C.; Bach, R. E.; and Mehta, R. S. 1984: Identification of Vortex-Induced Clear Air Turbulence Using Airline Flight Records. *J. Aircraft*, **22**, 124–129.
- Reed, R. J.; and Hardy, K. R. 1972: A Case Study of Persistent, Intense Clear-Air Turbulence in an Upper-Level Frontal Zone. *J. Appl. Meteor.*, **11**, 541–549.
- Reiter, E. R.; and Nania, A. 1964: Jet-Stream Structure and Clear-Air Turbulence. *J. Appl. Meteor.*, **3**, 247–260.
- Roach, W. T. 1970: On the Influence of Synoptic Development on the Influence of High Level Turbulence. *Quart. J. Roy. Meteor. Soc.*, **96**, 413–429.
- Shapiro, M. A. 1976: The Role of Turbulent Heat Flux in the Generation of Potential Vorticity in the Vicinity of Upper-Level Jet Stream Systems. *Mon. Wea. Rev.*, **104**, 892–906.
- Sharman, R.; Wiener, G.; and Brown, B. 2000: Description and Integration of the NCAR Integrated Turbulence Forecasting Algorithm (ITFA). AIAA 00-0493.
- Stone, P. H. 1966: On Non-Geostrophic Baroclinic Stability. *J. Atmos. Sci.*, **23**, 390–400.
- Uccellini, L. W.; Brill, K. F.; Petersen, R. A.; Keyser, D.; Aune, R.; Kocin, P. J.; and des Jardins, M. 1986: A Report on the Upper-Level Wind Conditions Preceding and During the Shuttle Challenger (STS 51L) Explosion. *Bull. Amer. Meteor. Soc.*, **67**, 1248–1265.

Table 1. MASS Model (Version 5.13) Characteristics

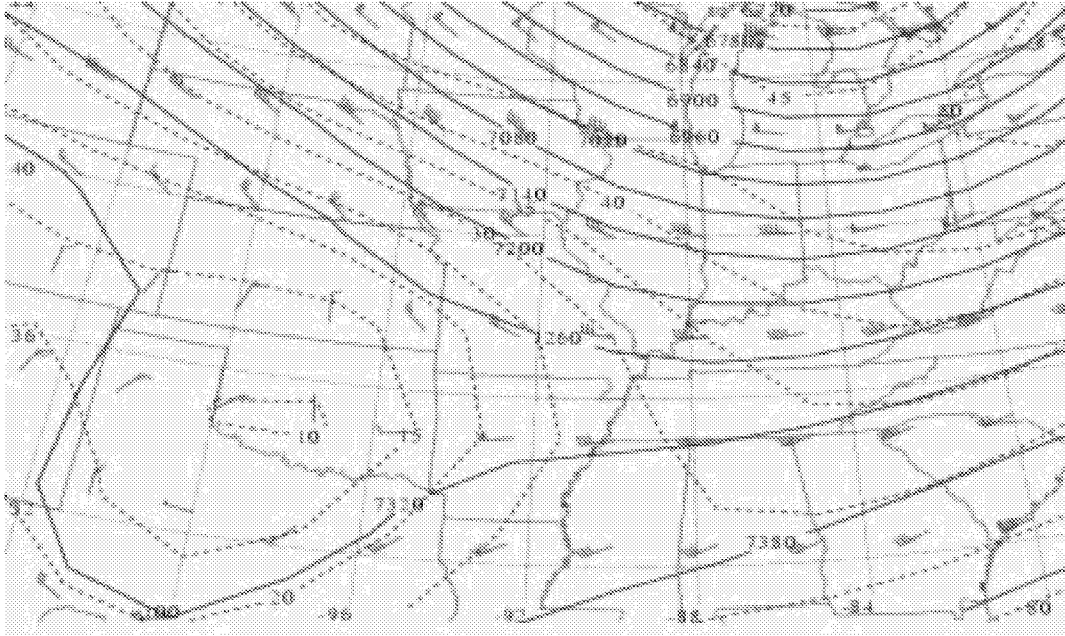
<p>Model Numerics</p>	<p>Hydrostatic primitive equation model 3-D equations for u, v, T, q, and p Cartesian grid on a polar stereographic map Sigma-p terrain-following vertical coordinate Vertical coverage from ~10m to ~16,000m Energy-absorbing sponge layer near model top Fourth-order horizontal space differencing on an unstaggered grid Split-explicit time integration schemes: (a) forward backward for the gravity mode and (b) Adams-Bashforth for the advective mode Time-dependent lateral boundary conditions Positive-definite advection scheme for the scalar variables Massless tracer equations for ozone and aerosol transport</p>
<p>Initialization</p>	<p>First guess from large-scale gridded analyses Reanalysis with rawinsonde and surface data using a 3D optimum interpolation scheme High-resolution terrain data base derived from observations High-resolution satellite or climatological sea surface temperature database High-resolution land use classification scheme High-resolution climatological subsoil moisture data base derived from antecedent precipitation High resolution normalized difference vegetation index</p>
<p>PBL Specification</p>	<p>Blackadar PBL scheme Surface energy budget Soil hydrology scheme Atmospheric radiation attenuation scheme</p>
<p>Moisture Physics</p>	<p>Grid-scale prognostic equations for cloud water and ice, rainwater, and snow Kain-Fritsch convective parameterization</p>

Table 2. Data for the Four Hydrostatic Simulations

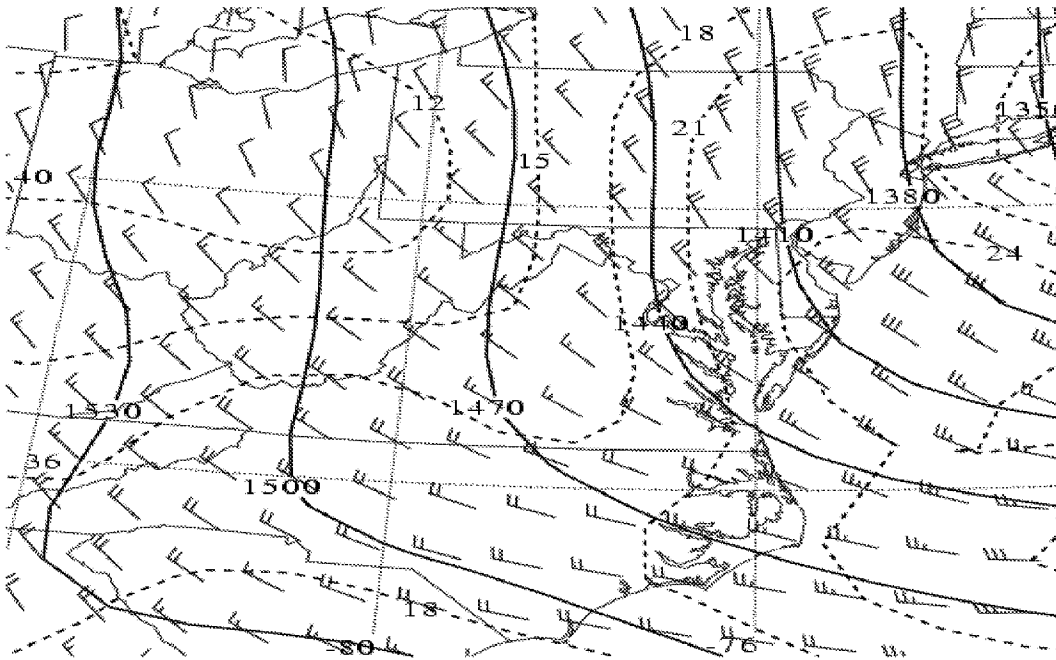
Case	Simulation	Horizontal Resolution	Vertical Resolution	Initialization Time	Grid Dimensions
Cape Girardeau	1	30 km	45	0000 UTC 1/28/97	130 × 100
	2	12 km	45	0600 UTC 1/28/97	130 × 100
	3	6 km	60	1000 UTC 1/28/97	200 × 200
Valdosta	1	30 km	50	0000 UTC 12/14/00	100 × 100
	2	6 km	50	1000 UTC 12/14/00	100 × 100
Cross City	1	30 km	35	0000 UTC 10/1/97	140 × 130
	2	18 km	35	0000 UTC 10/1/97	140 × 130
	3	6 km	35	1500 UTC 10/1/97	120 × 100
Wilmington	1	30 km	50	0000 UTC 1/13/00	100 × 100
	2	15 km	50	0600 UTC 1/13/00	170 × 170
	3	6 km	50	1200 UTC 1/13/00	200 × 200

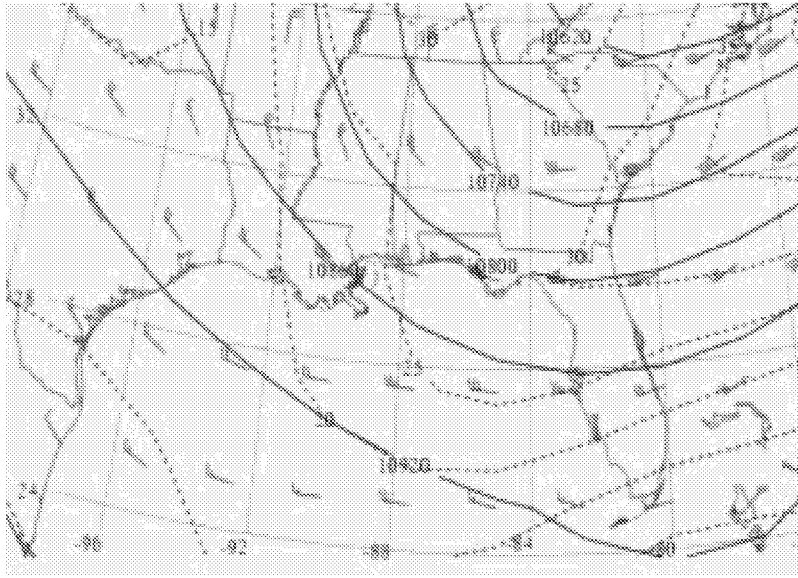
Table 3. Information About the Turbulence Encounter for Each of the Four Case Studies

Approximate accident location	Date	Time of turbulence encounter	Pressure level of turbulence
Cape Girardeau, Mo	1/28/97	1453 UTC	400 mb
Valdosta, Ga	12/14/00	1844 UTC	250 mb
Cross City, Fl	10/2/97	0045 UTC	275 mb
Wilmington, De	1/13/00	1931 UTC	775 mb

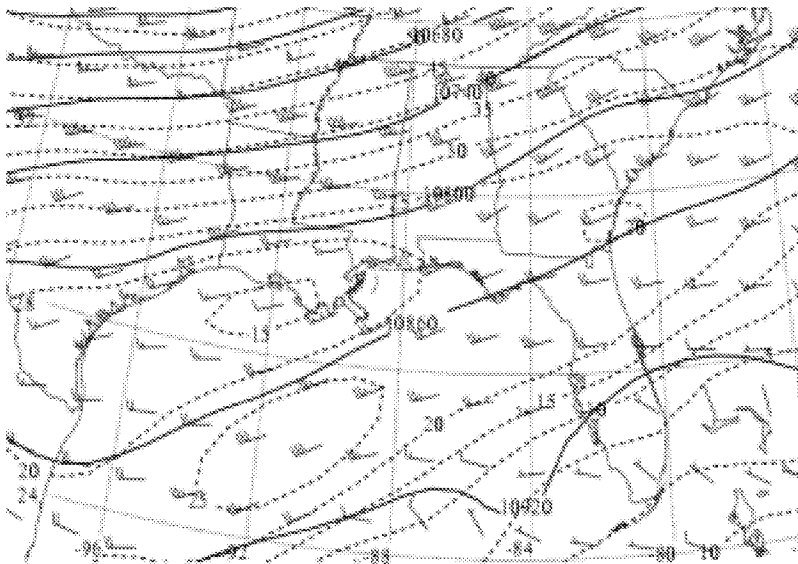


(a) Valid at the observation time preceding the accident for the CGI case study at 400 hPa and valid at 1200 UTC 28 January 1997.



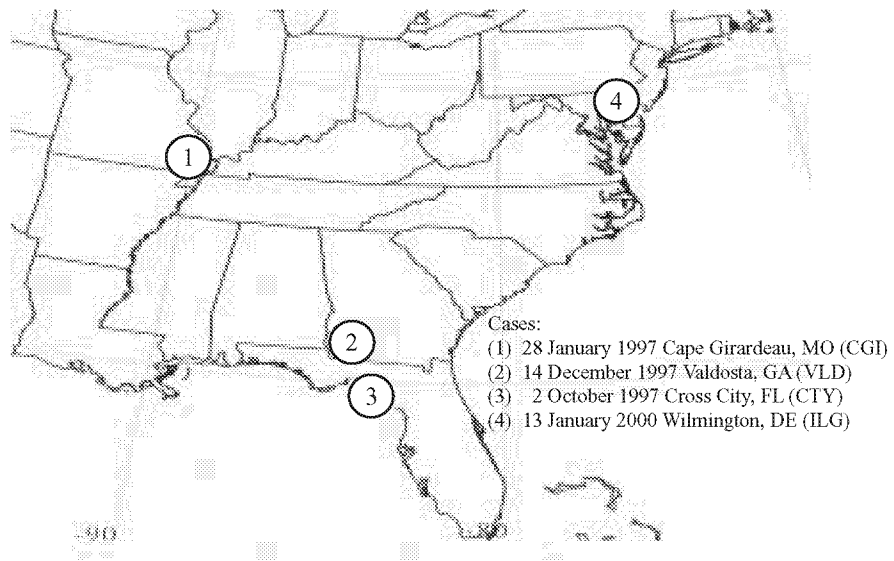


(c) Valid at the observation time preceding the accident for the CTY case study at 250 hPa and valid at 0000 UTC 2 October 1997.



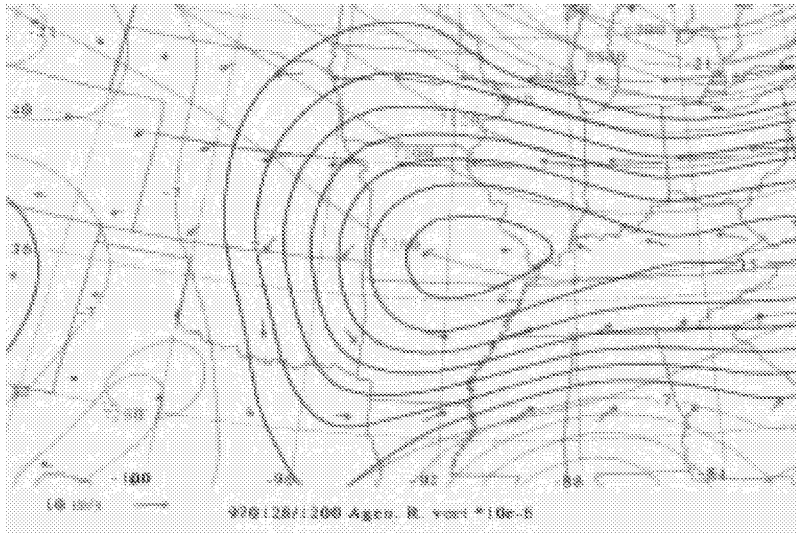
(d) Valid at the observation time preceding the accident for the VLD case study at 250 hPa and valid at 1200 UTC 14 December 2000.

Figure 1. Continued.

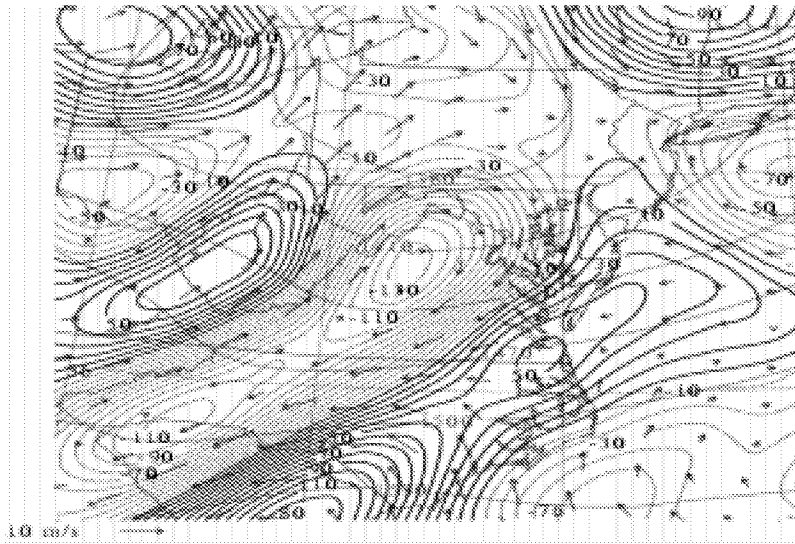


(e) Locations of turbulence reports for the 4 case studies.

Figure 1. Concluded.

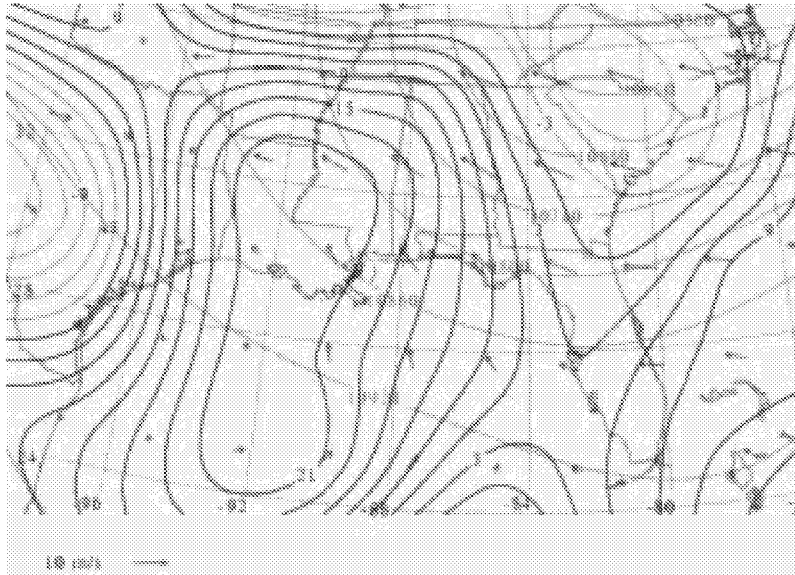


(a) NCEP Reanalysis 400 hPa 1200 UTC 28 January 1997.

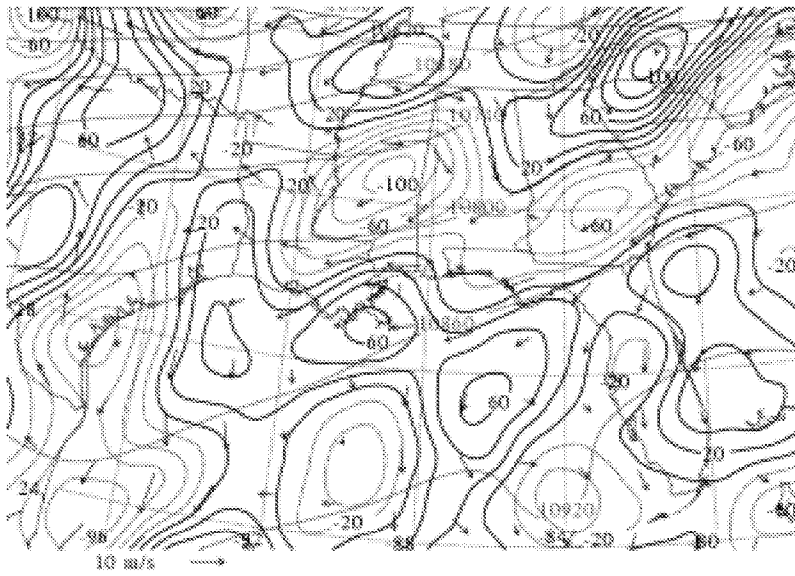


(b) Eta 850 hPa 0000 UTC 14 January 2000.

Figure 2. NCEP height (light solid in m), ageostrophic wind vectors, and ageostrophic relative vorticity (negative dashed and positive dark solid in $s^{-1} \times 10^{-6}$).

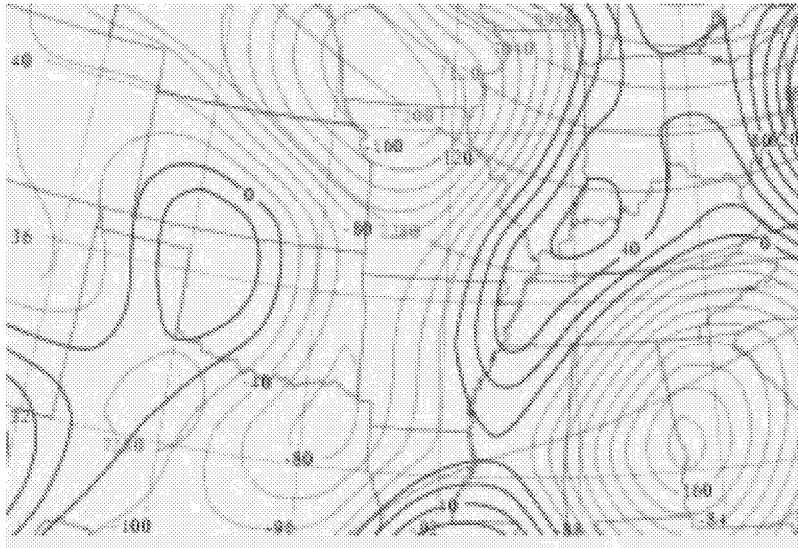


(c) NCEP Reanalysis 250 hPa 0000 UTC 2 October 1997.

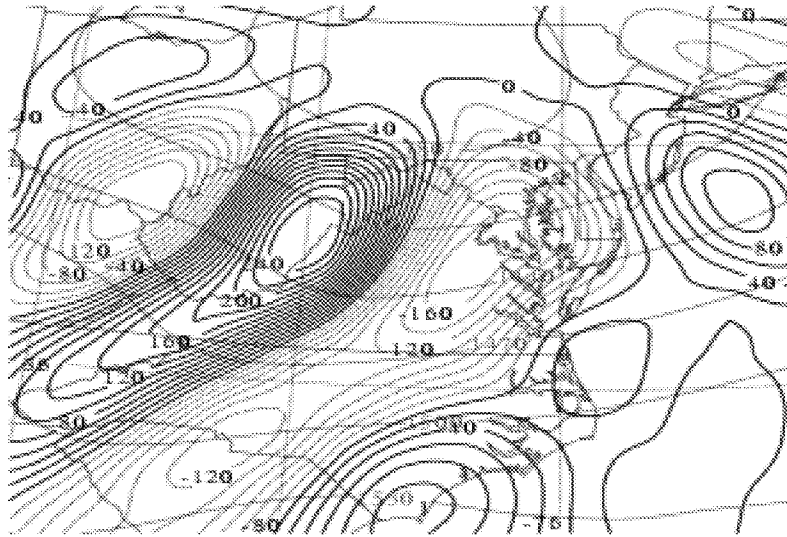


(d) Eta 250 hPa 1200 UTC 14 December 2000.

Figure 2. Concluded.

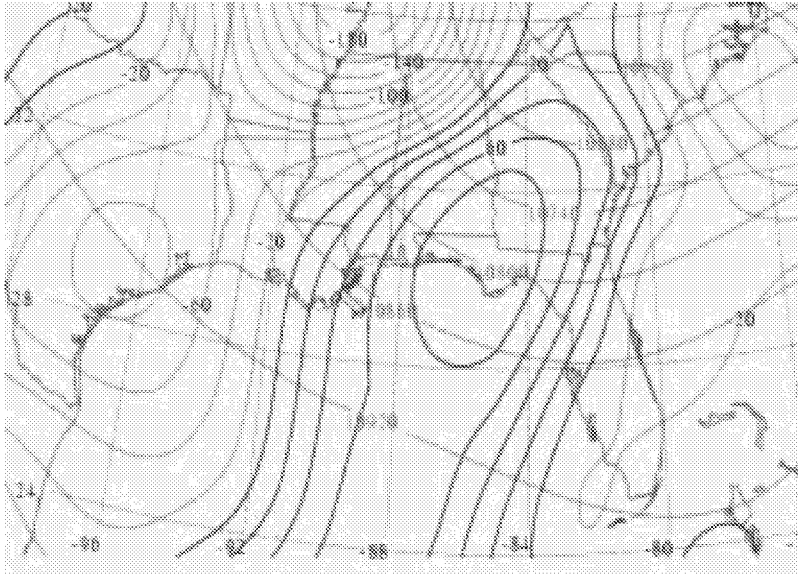


(a) NCEP Reanalysis 400 hPa 1200 UTC 28 January 1997.

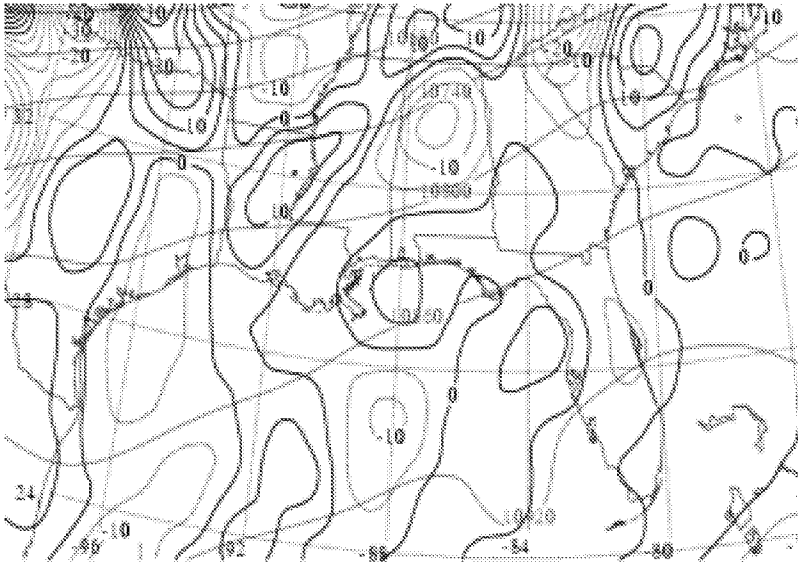


(b) Eta 850 hPa 0000 UTC 14 January 2000.

Figure 3. NCEP height (light solid in m) and ageostrophic relative vorticity advection (negative dashed and positive dark solid in $s^{-2} \times 10^{-10}$).

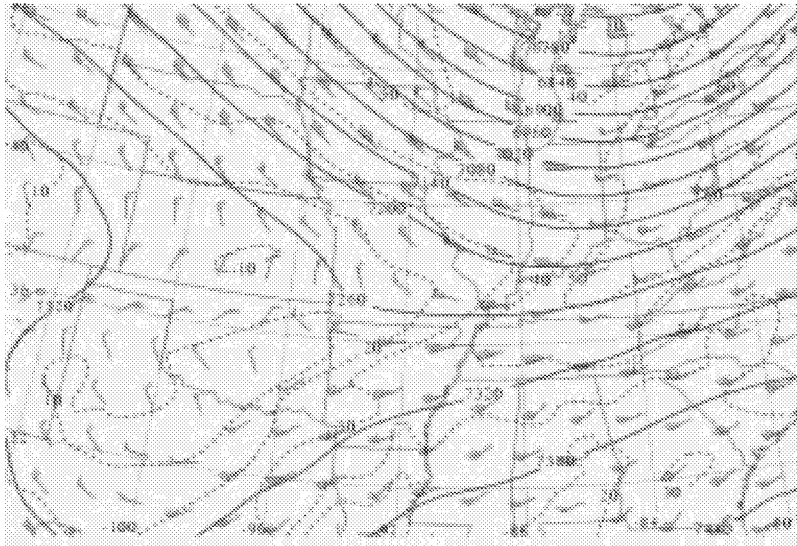


(c) NCEP Reanalysis 250 hPa 0000 UTC 2 October 1997.

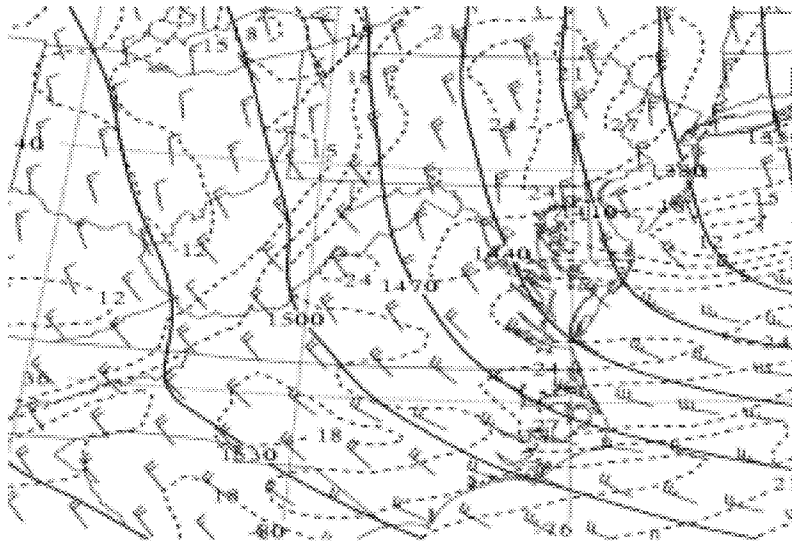


(d) Eta 250 hPa 1200 UTC 14 December 2000 ($s^{-2} \times 10^{-9}$).

Figure 3. Concluded.

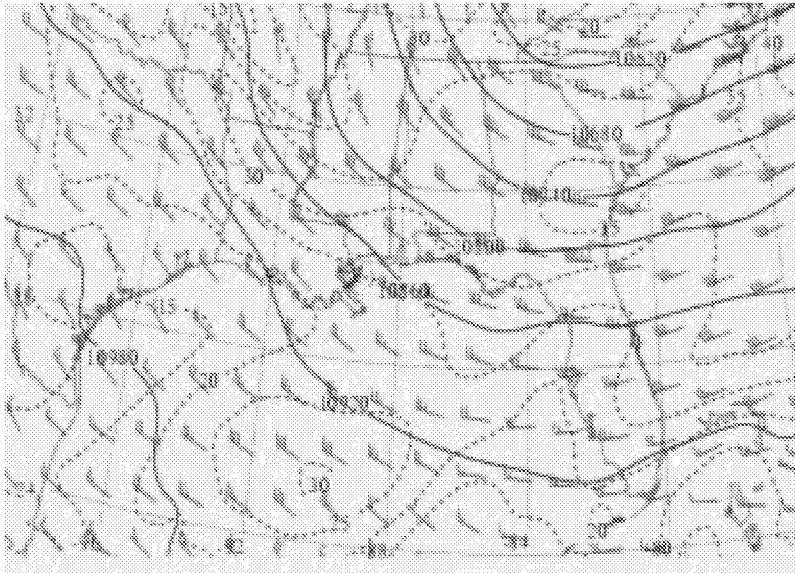


(a) Valid on/at 400 hPa 1200 UTC 28 January 1997.

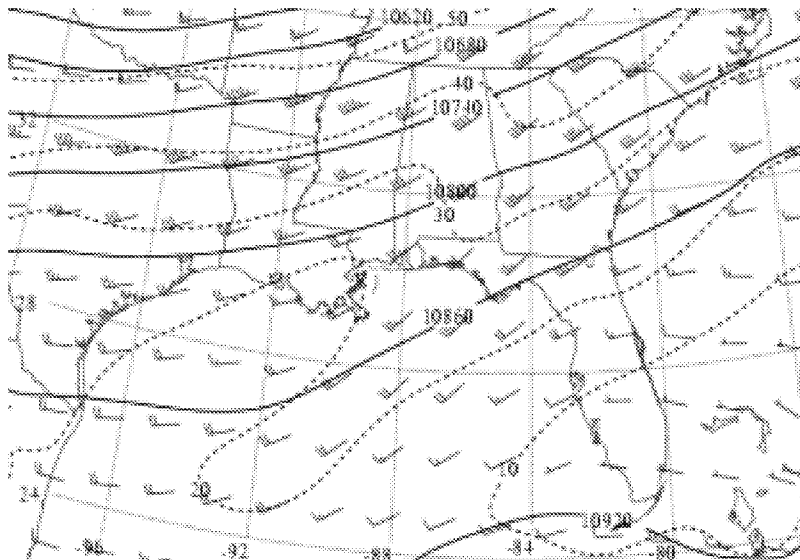


(b) Valid on/at 850 hPa 0000 UTC 14 January 2000.

Figure 4. MASS 30-km simulated total wind isotachs (dashed in ms^{-1}), wind barbs (short barb = 5 ms^{-1} ; long barb = 10 ms^{-1} ; triangle = 50 ms^{-1}), and heights (solid in m).

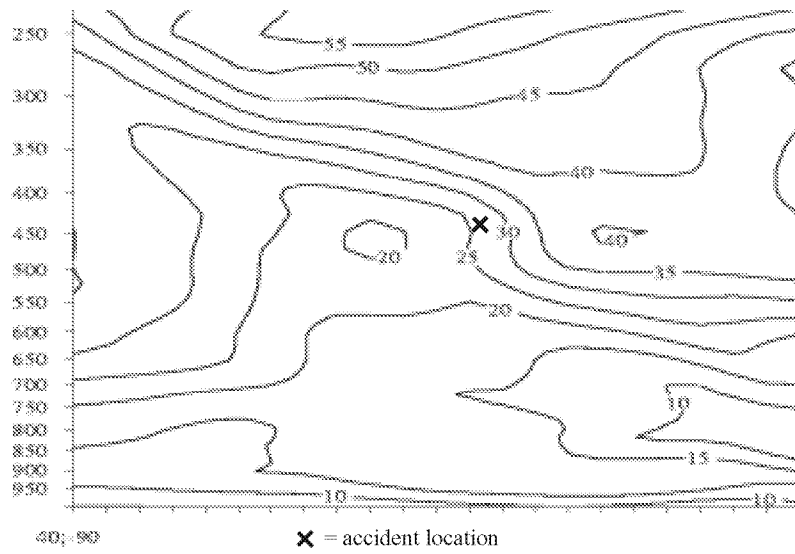


(c) Valid on/at 250 hPa 0000 UTC 2 October 1997.

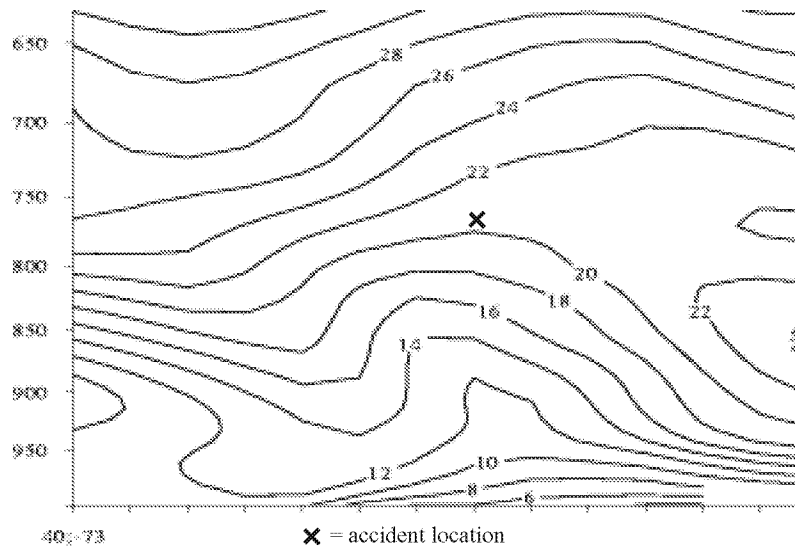


(d) Valid on/at 250 hPa 1200 UTC 14 December 2000.

Figure 4. Concluded.

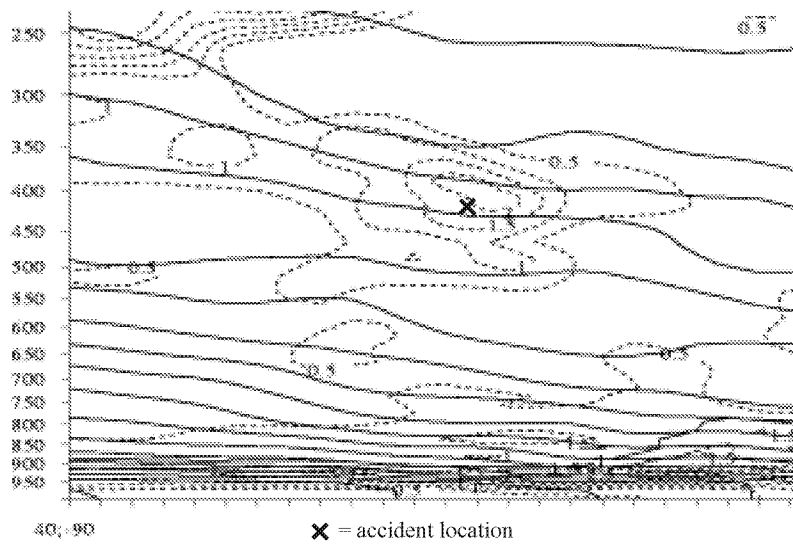


(a) Valid at 1200 UTC 28 January 1997.

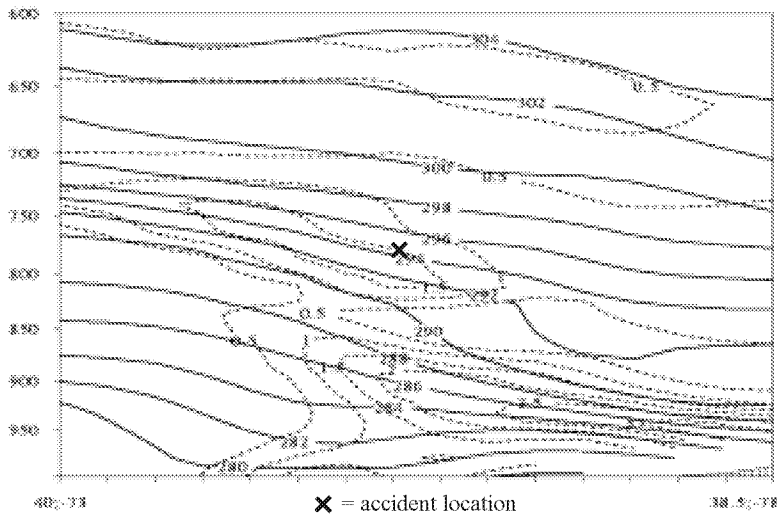


(b) Valid at 1800 UTC 13 January 2000.

Figure 5. MASS 30-km simulated jet normal vertical cross sections of total wind isotachs (solid in ms^{-1}).

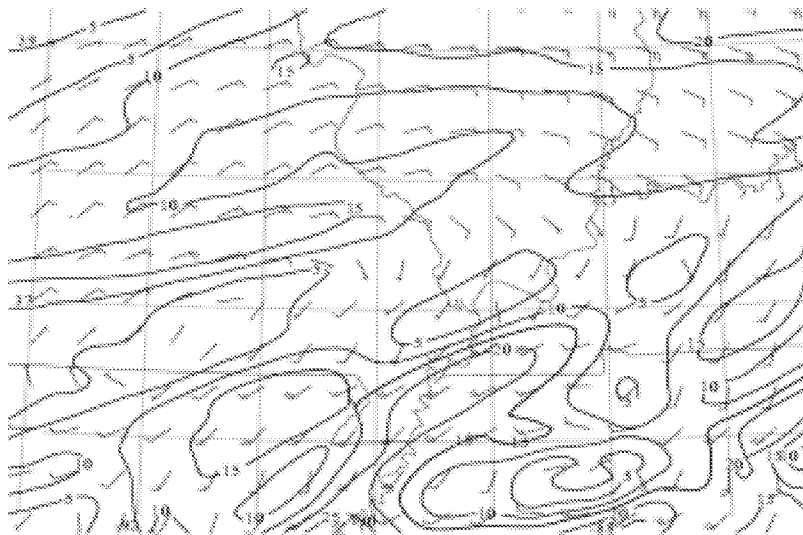


(a) Valid at 1200 UTC 28 January 1997.

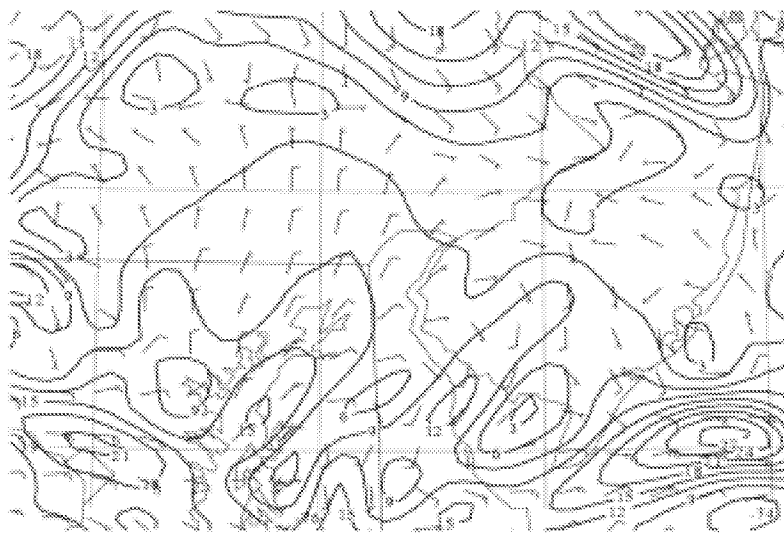


(b) Valid at 1800 UTC 13 January 1997.

Figure 6. MASS 30-km simulated jet normal vertical cross sections of potential temperature (solid in K) and isentropic potential vorticity (dashed in $\text{Kmb}^{-1}\text{s}^{-1} \times 10^{-6}$).

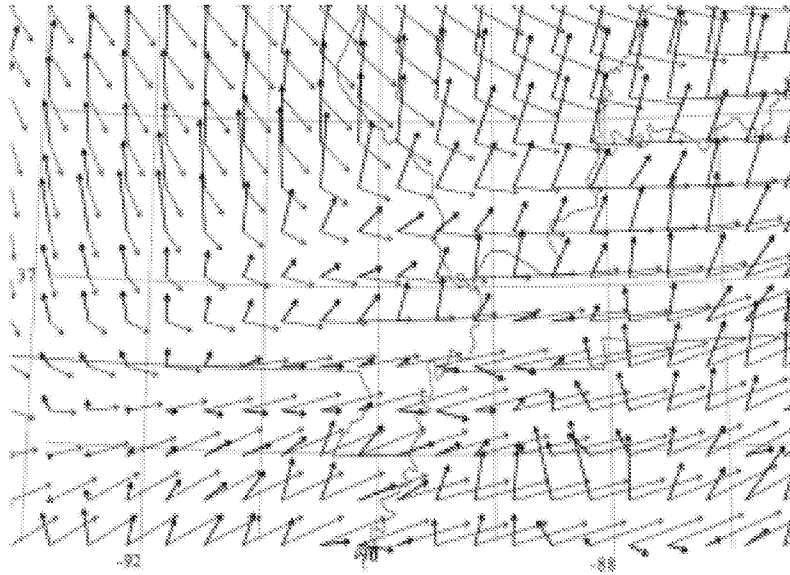


(a) Valid on/at 400 hPa 1330 UTC 28 January 1997.

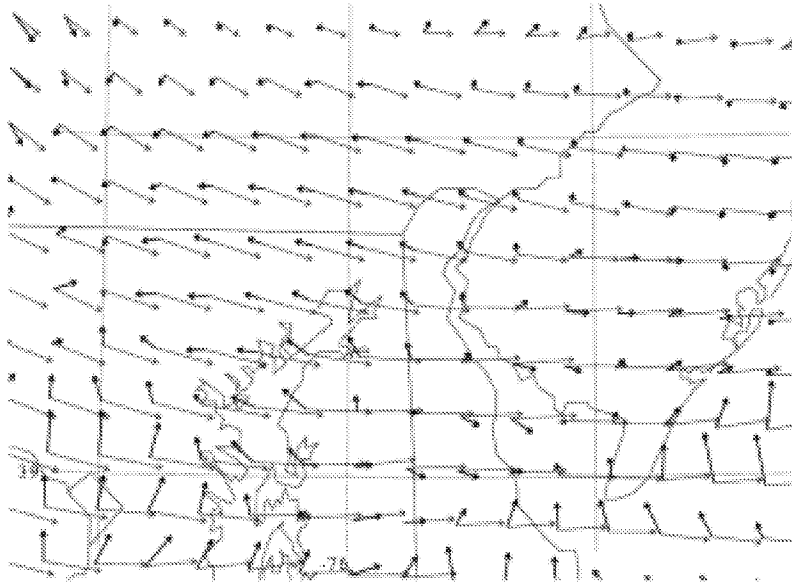


(b) Valid on/at 775 hPa 1900 UTC 13 January 2000.

Figure 7. MASS 6-km simulated ageostrophic wind isotachs (solid in ms^{-1}) and vectors.

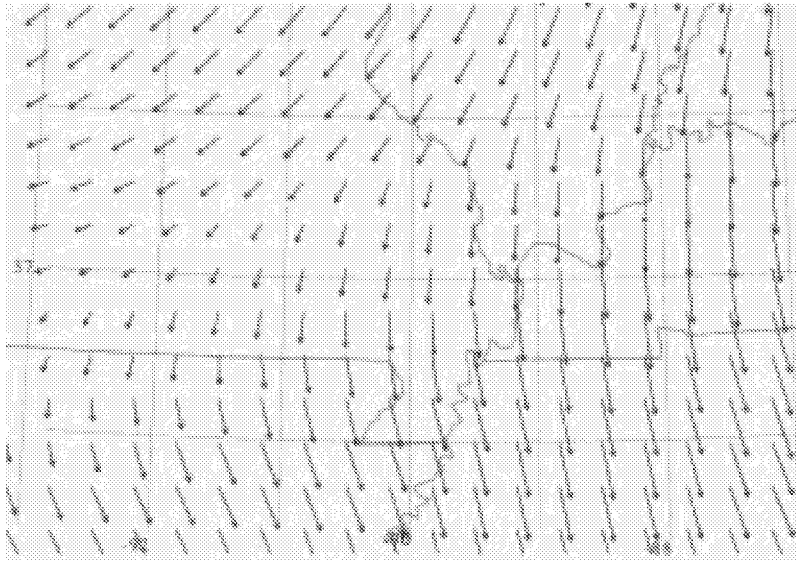


(a) Valid at 400 hPa 1330 UTC 28 January 1997.

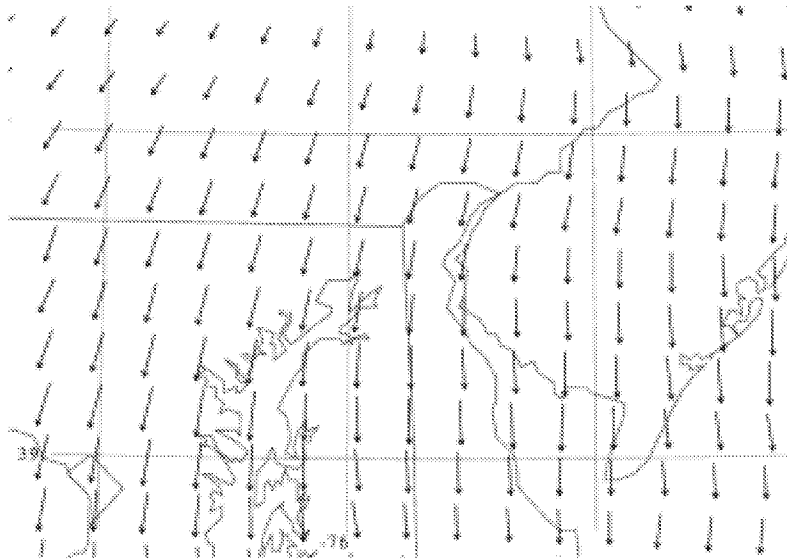


(b) 775 hPa 1900 UTC 13 January 2000.

Figure 8. MASS 6-km simulated vector resultant of the pressure gradient force and Coriolis force (thick) versus the total wind vectors (thin).

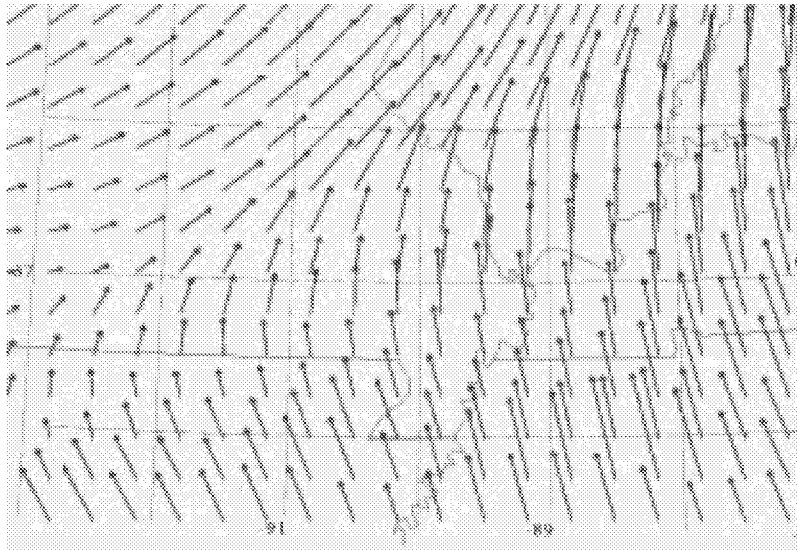


(a) Valid on/at 400 hPa 1330 UTC 28 January 1997.

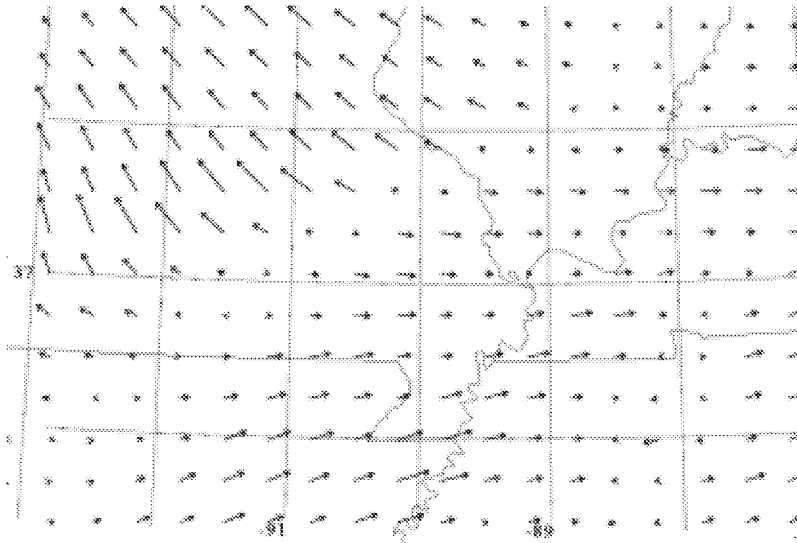


(b) Valid on/at 775 hPa 1900 UTC 13 January 2000.

Figure 9. MASS 6-km simulated Coriolis force vectors.

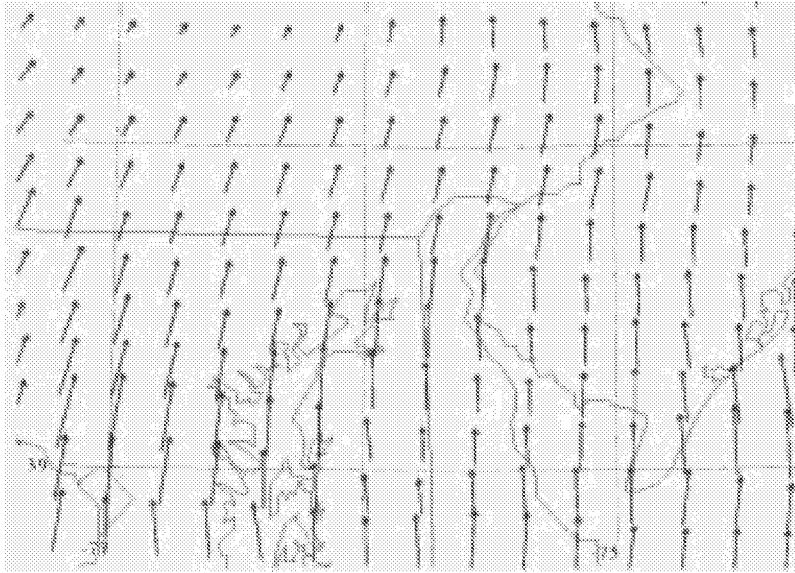


(a) Valid on/at 400 hPa 1330 UTC 28 January 1997.

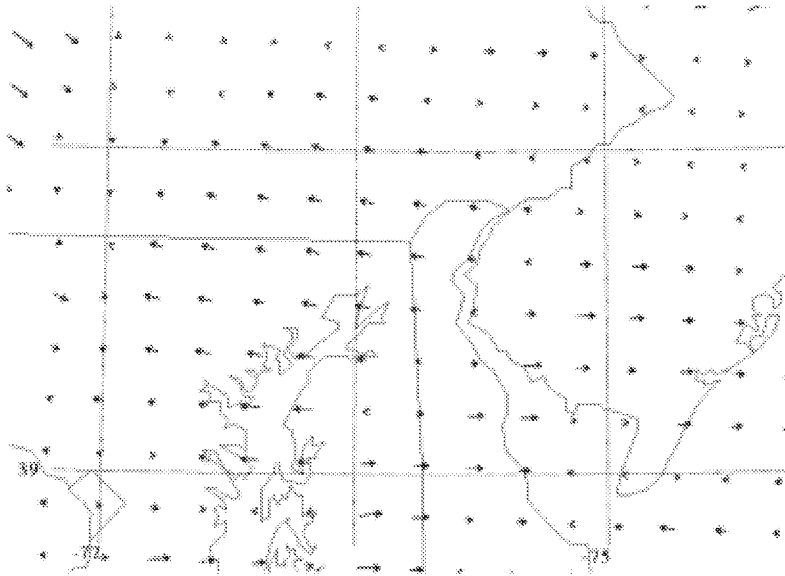


(b) Valid on/at 400 hPa 1330 UTC 28 January 1997.

Figure 10. MASS 6-km simulated cross-stream component and along-stream components of the pressure gradient force vectors.

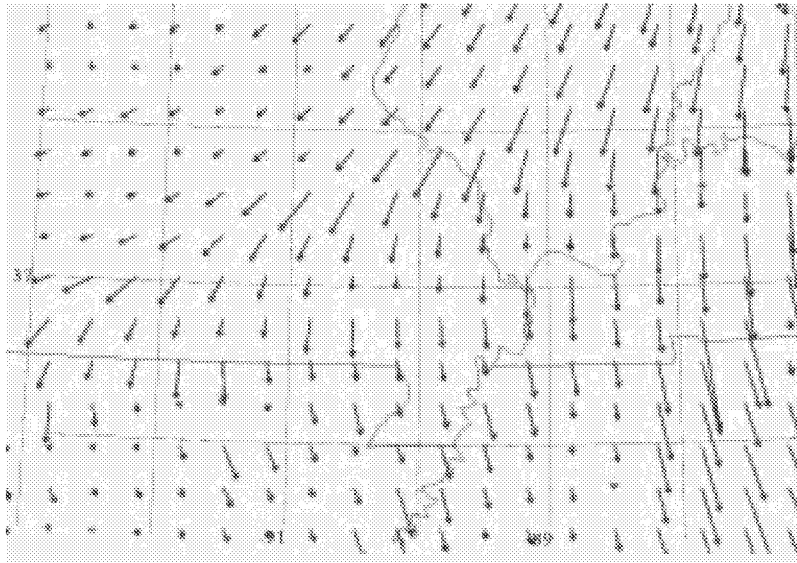


(c) Valid on/at 775 hPa 1900 UTC 13 January 1997.

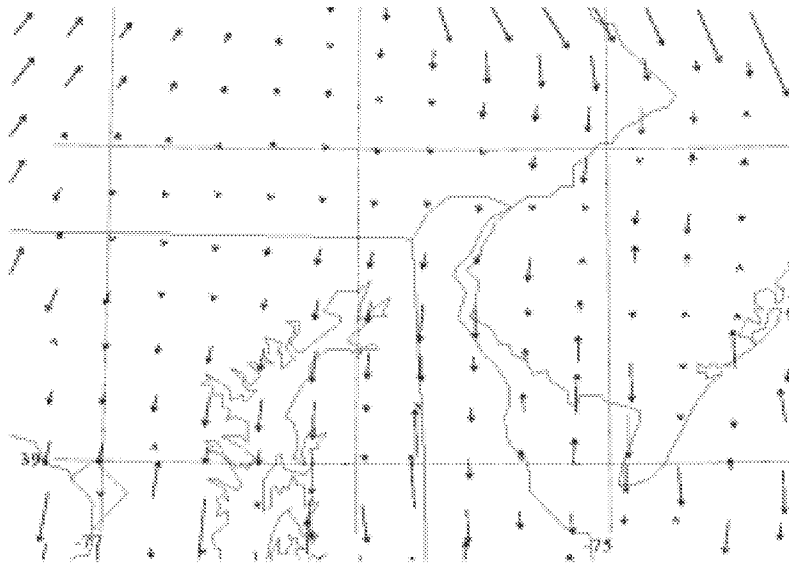


(d) Valid on/at 775 hPa 1900 UTC 13 January 1997.

Figure 10. Concluded.

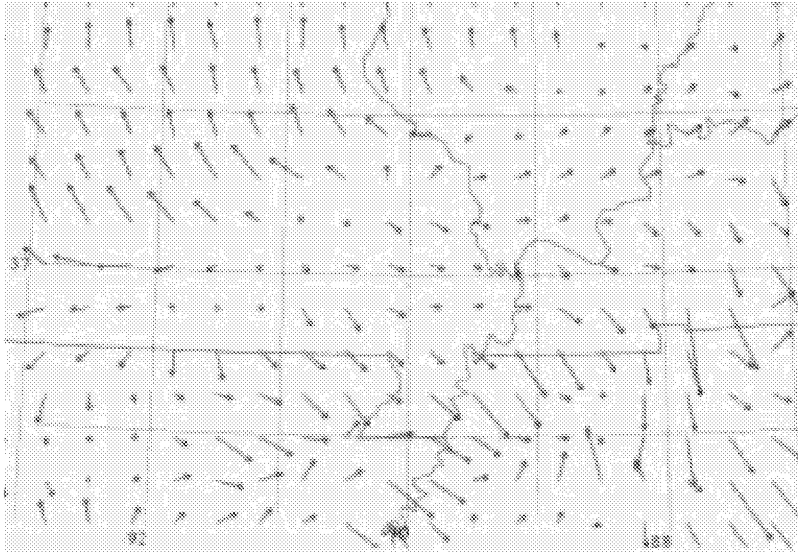


(a) Valid on/at 400 hPa 1330 UTC 28 January 1997.

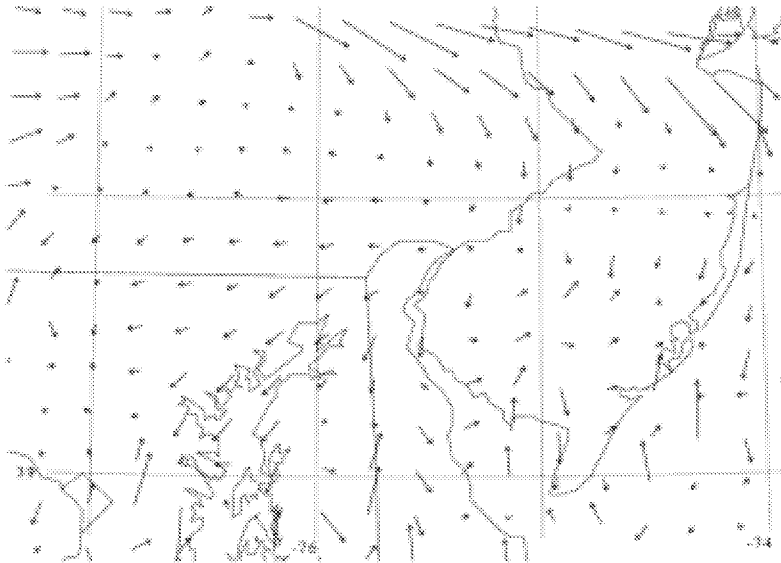


(b) Valid on/at 775 hPa 1900 UTC 13 January 2000.

Figure 11. MASS 6-km simulated centrifugal force vectors.

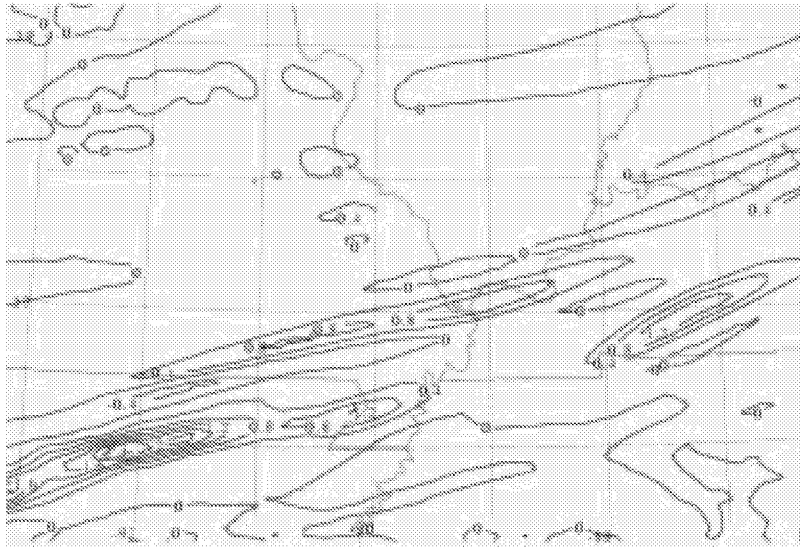


(a) Valid on/at 400 hPa 1330 UTC 28 January 1997.

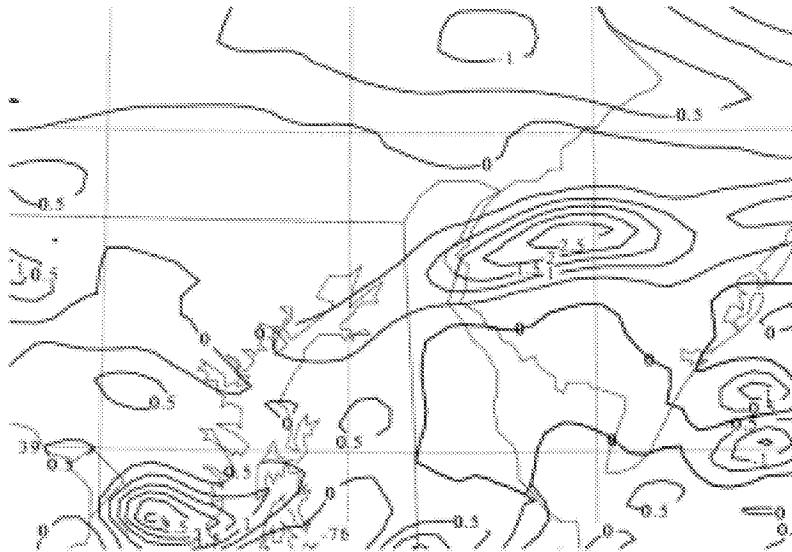


(b) Valid on/at 775 hPa 1900 UTC 13 January 2000.

Figure 12. MASS 6-km simulated resultant of all four force vectors.

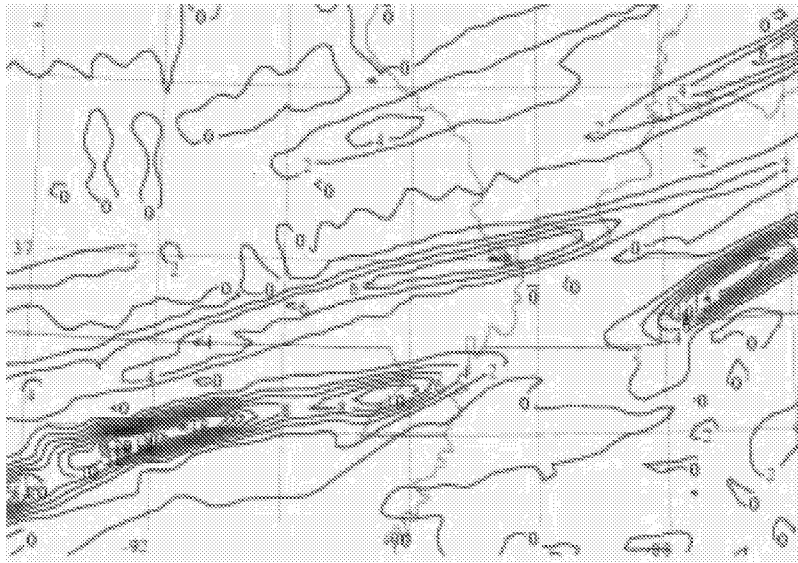


(a) Valid on/at 400 hPa 1330 UTC 28 January 1997.

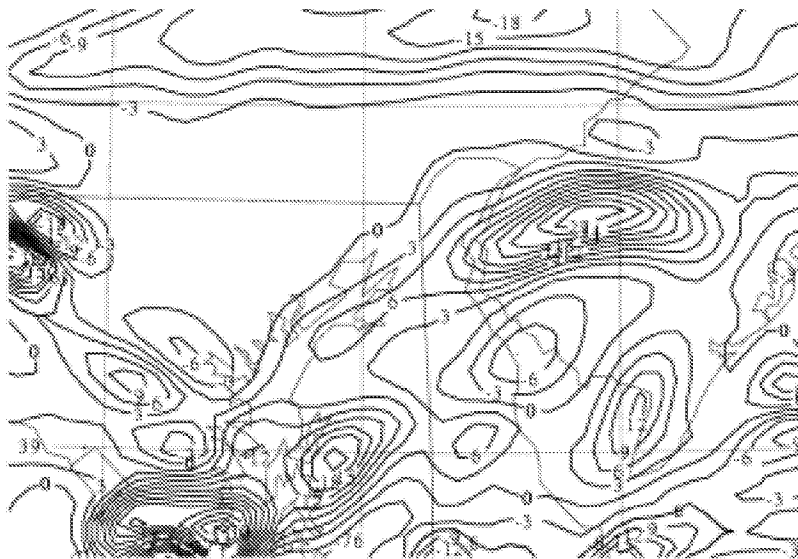


(b) Valid on/at 775 hPa 1900 UTC 13 January 2000.

Figure 13. MASS 6-km simulated v wind component divergence forcing function term in Miller's frontogenesis equation ($\text{km}^{-1}\text{s}^{-1} \times 10^{-8}$).

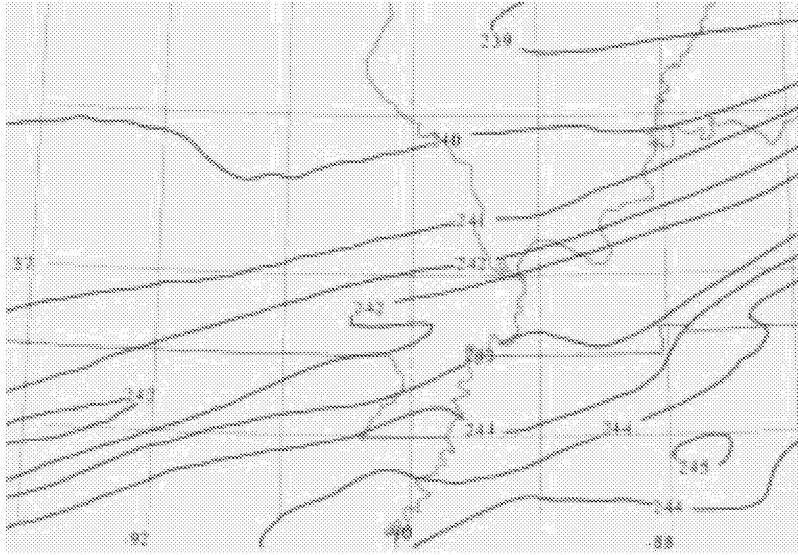


(a) Valid on/at 400 hPa 1330 UTC 28 January 1997.

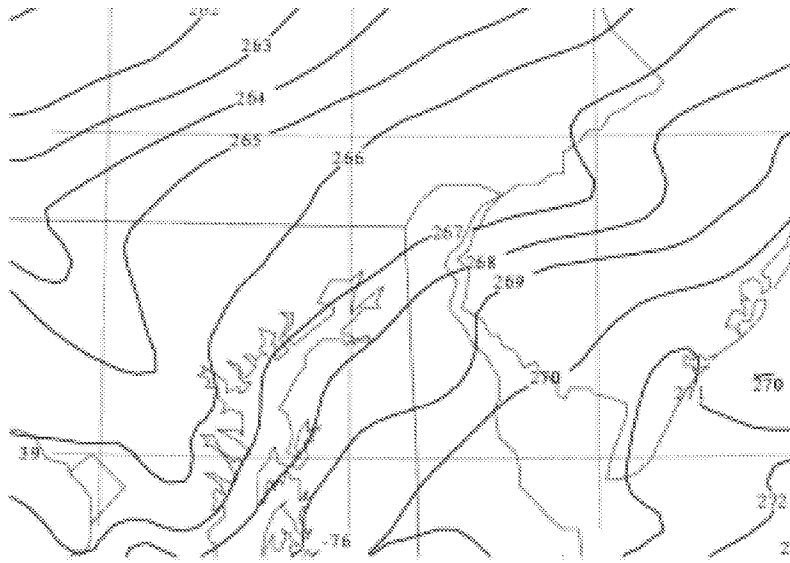


(b) Valid on/at 775 hPa 1900 UTC 13 January 2000.

Figure 14. MASS 6-km simulated total frontogenesis from Miller's (1957) equation ($\text{km}^{-1}\text{s}^{-1} \times 10^{-8}$).

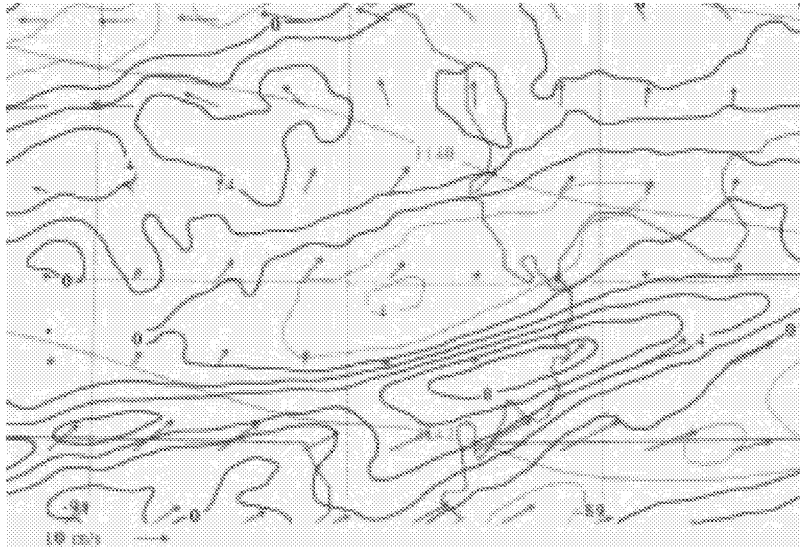


(a) Valid on/at 400 hPa 1330 UTC 28 January 1997.

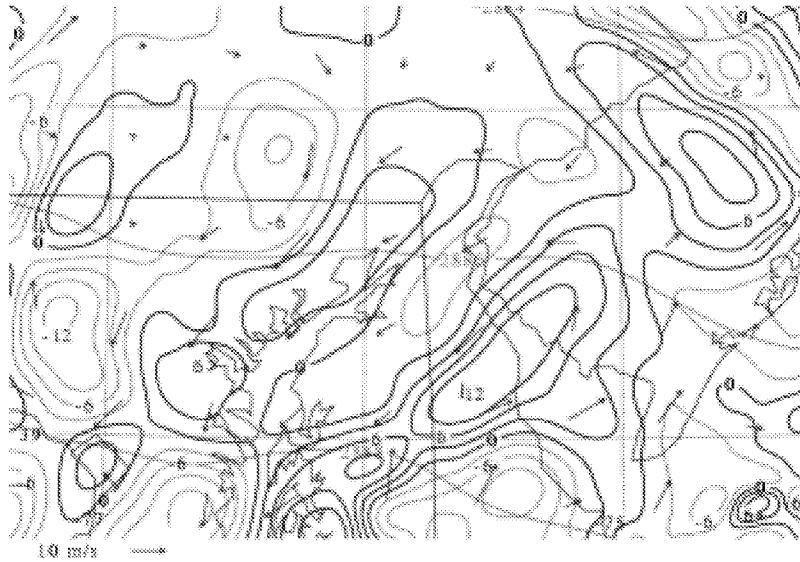


(b) Valid on/at 775 hPa 1900 UTC 13 January 2000.

Figure 15. MASS 6-km simulated temperature (K).



(a) Valid on/at 314 K 1330 UTC 28 January 1997.

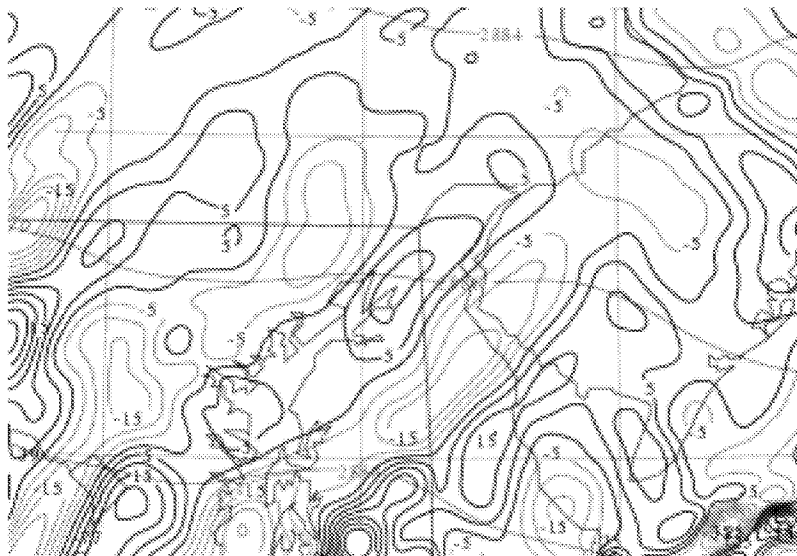


(b) Valid on/at 287 K 1900 UTC 13 January 2000.

Figure 16. MASS 6-km simulated Montgomery stream function (light solid in m^2s^{-2}), ageostrophic wind vectors, and ageostrophic z-space relative vorticity ($\text{s}^{-1} \times 10^{-4}$).

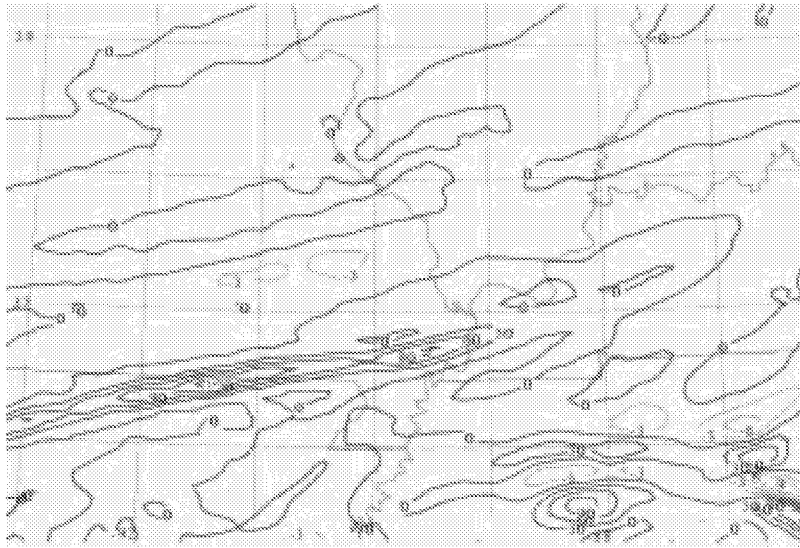


(a) Valid on/at 314 K 1330 UTC 28 January 1997.

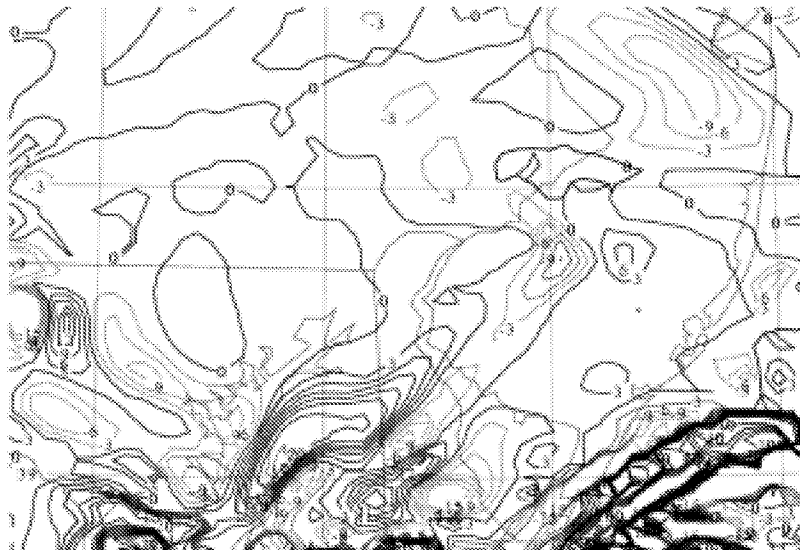


(b) Valid on/at 287 K 1900 UTC 13 January 2000.

Figure 17. MASS 6-km simulated velocity divergence term in the ageostrophic z-space relative vorticity equation ($s^{-2} \times 10^{-9}$ in (a), $s^{-2} \times 10^{-7}$ in (b)) on an isentropic surface.



(a) Valid on/at 314 K 1330 UTC 28 January 1997.



(b) Valid on/at 287 K 1900 UTC 13 January 2000.

Figure 18. MASS 6-km simulated Montgomery stream function (light solid in m^2s^{-2}) and the advection of ageostrophic z-space relative vorticity ($\text{s}^{-1} \times 10^{-8}$).

REPORT DOCUMENTATION PAGE			Form Approved OMB No. 0704-0188		
<p><i>The public reporting burden for this collection of information is estimated to average 1 hour per response, including the time for reviewing instructions, searching existing data sources, gathering and maintaining the data needed, and completing and reviewing the collection of information. Send comments regarding this burden estimate or any other aspect of this collection of information, including suggestions for reducing this burden, to Department of Defense, Washington Headquarters Services, Directorate for Information Operations and Reports (0704-0188), 1215 Jefferson Davis Highway, Suite 1204, Arlington, VA 22202-4302. Respondents should be aware that notwithstanding any other provision of law, no person shall be subject to any penalty for failing to comply with a collection of information if it does not display a currently valid OMB control number.</i></p> <p>PLEASE DO NOT RETURN YOUR FORM TO THE ABOVE ADDRESS.</p>					
1. REPORT DATE (DD-MM-YYYY) 02-2003		2. REPORT TYPE Contractor Report		3. DATES COVERED (From - To)	
4. TITLE AND SUBTITLE Characterizing the Severe Turbulence Environments Associated With Commercial Aviation Accidents <i>Part II: Hydrostatic Mesobeta Scale Numerical Simulations of Supergradient Wind Flow and Streamwise Ageostrophic Frontogenesis</i>			5a. CONTRACT NUMBER NAS1-99074		
			5b. GRANT NUMBER		
			5c. PROGRAM ELEMENT NUMBER		
6. AUTHOR(S) Kaplan, Michael L.; Huffman, Allan W.; Lux, Kevin M.; Cetola, Jeffrey D.; Charney, Joseph J.; Riordan, Allen J.; Lin, Yuh-Lang; and Waight, Kenneth T., III			5d. PROJECT NUMBER		
			5e. TASK NUMBER		
			5f. WORK UNIT NUMBER 728-40-30-01		
7. PERFORMING ORGANIZATION NAME(S) AND ADDRESS(ES) Research Triangle Institute Research Triangle Park, NC 27709			8. PERFORMING ORGANIZATION REPORT NUMBER		
9. SPONSORING/MONITORING AGENCY NAME(S) AND ADDRESS(ES) National Aeronautics and Space Administration Langley Research Center Hampton, VA 23681-2199			10. SPONSOR/MONITOR'S ACRONYM(S) NASA		
			11. SPONSOR/MONITOR'S REPORT NUMBER(S) NASA/CR-2003-212138		
12. DISTRIBUTION/AVAILABILITY STATEMENT Unclassified - Unlimited Subject Category 03 Availability: NASA CASI (301) 621-0390 Distribution: Standard					
13. SUPPLEMENTARY NOTES Kaplan, Huffman, Lux, Cetola, Riordan, and Lin: North Carolina State Univ., Raleigh, NC. Charney: North Central Res. Stat., East Lansing, MI. Waight: MESO Inc., Raleigh, NC. Electronic version: http://techreports.larc.nasa.gov/ltrs/ or http://techreports.larc.nasa.gov/cgi-bin/NTRS Langley Technical Monitor: Fred Proctor.					
14. ABSTRACT Simulation experiments reveal key processes that organize a hydrostatic environment conducive to severe turbulence. The paradigm requires juxtaposition of the entrance region of a curved jet stream, which is highly subgeostrophic, with the entrance region of a straight jet stream, which is highly supergeostrophic. The wind and mass fields become misphased as the entrance regions converge resulting in the significant spatial variation of inertial forcing, centripetal forcing, and along- and cross-stream pressure gradient forcing over a mesobeta scale region. This results in frontogenesis and the along-stream divergence of cyclonic and convergence of cyclonic ageostrophic vertical vorticity. The centripetally forced mesoscale front becomes the locus of large gradients of ageostrophic vertical vorticity along an overturning isentrope. This region becomes favorable for streamwise vorticity gradient formation enhancing the environment for organization of horizontal vortex tubes in the presence of buoyant forcing.					
15. SUBJECT TERMS Turbulence; Convection; Vorticity; Wind shear; Jet stream					
16. SECURITY CLASSIFICATION OF:			17. LIMITATION OF ABSTRACT	18. NUMBER OF PAGES	19a. NAME OF RESPONSIBLE PERSON
a. REPORT	b. ABSTRACT	c. THIS PAGE			STI Help Desk (email: help@sti.nasa.gov)
U	U	U	UU	45	19b. TELEPHONE NUMBER (Include area code) (301) 621-0390